
REFLECTED SCHRÖDINGER BRIDGE FOR CONSTRAINED GENERATIVE MODELING

A PREPRINT

Wei Deng*, **Yu Chen***
Machine Learning Research
Morgan Stanley

Nicole Tianjiao Yang*, **Hengrong Du***, **Qi Feng**
Department of Mathematics
{Emory, Vanderbilt, Florida State} University

Ricky T. Q. Chen
Meta AI (FAIR)

January 9, 2024

ABSTRACT

Diffusion models have become the go-to method for large-scale generative models in real-world applications. These applications often involve data distributions confined within bounded domains, typically requiring ad-hoc thresholding techniques for boundary enforcement. Reflected diffusion models [Lou and Ermon, 2023] aim to enhance generalizability by generating the data distribution through a backward process governed by reflected Brownian motion. However, reflected diffusion models may not easily adapt to diverse domains without the derivation of proper diffeomorphic mappings and do not guarantee optimal transport properties. To overcome these limitations, we introduce the Reflected Schrödinger Bridge algorithm—an entropy-regularized optimal transport approach tailored for generating data within diverse bounded domains. We derive elegant reflected forward-backward stochastic differential equations with Neumann and Robin boundary conditions, extend divergence-based likelihood training to bounded domains, and explore natural connections to entropic optimal transport for the study of approximate linear convergence—a valuable insight for practical training. Our algorithm yields robust generative modeling in diverse domains, and its scalability is demonstrated in real-world constrained generative modeling through standard image benchmarks.

1 Introduction

Iterative refinement is key to the unprecedented success of diffusion models. They exhibit statistical efficiency [Koehler et al., 2023] and reduced dimensionality dependence [Vono et al., 2022], driving innovation in image, audio, video, and molecule synthesis [Dhariwal and Nichol, 2022, Ho et al., 2022, Hooeboom et al., 2022, Bunne et al., 2023]. However, diffusion models do not inherently guarantee optimal transport properties [Lavenant and Santambrogio, 2022] and often result in slow inference [Ho et al., 2020, Salimans and Ho, 2022, Lu et al., 2022]. Furthermore, the consistent reliance on Gaussian priors imposes limitations on the application potential and sacrifices the efficiency when the data distribution significantly deviates from the Gaussian prior.

The predominant method for fast inference originates from the field of optimal transport (OT). Notably, the (static) iterative proportional fitting (IPF) algorithm [Kullback, 1968, Ruschendorf, 1995] addresses this challenge by employing alternating projections onto each marginal distribution. This algorithm has showcased impressive performance in low-dimensional contexts [Chen and Georgiou, 2016, Pavon et al., 2021, Caluya and Halder, 2022]. In contrast, the Schrödinger bridge (SB) problem [Léonard, 2014] introduces a principled framework for the dynamic treatment of entropy-regularized optimal transport (EOT) [Villani, 2003, Peyré and Cuturi, 2019]. Recent advances [De Bortoli et al., 2021, Chen et al., 2022b] have pushed the frontier of IPFs to (ultra-)high-dimensional generative models using deep neural networks (DNNs) and have generated straighter trajectories; Additionally, SBs based on Gaussian process [Vargas et al., 2021] demonstrates great promise in robustness and scalability; Bridge matching methods [Shi et al., 2023, Peluchetti, 2023] also offers promising alternatives for solving complex dynamic SB problems.

*Deng, Chen, Yang, and Du contributed equally to this work. Correspondence: weideng056@gmail.com

Real-world data, such as pixel values in images, often exhibits bounded support. To address this challenge, a common practice involves the use of thresholding techniques [Ho et al., 2020] to guide the sampling process towards the intended domain of simple structures. Lou and Ermon [2023] introduced reflected diffusion models that employ reflected Brownian motion on constrained domains such as hypercubes and simplex. However, constrained domains on general Euclidean space with optimal transport guarantee are still not well developed. Moreover, Lou and Ermon [2023] relies on a uniform prior based on variance-exploding (VE) SDE to derive closed-form scores, and the popular variance-preserving (VP) SDE is not fully exploited.

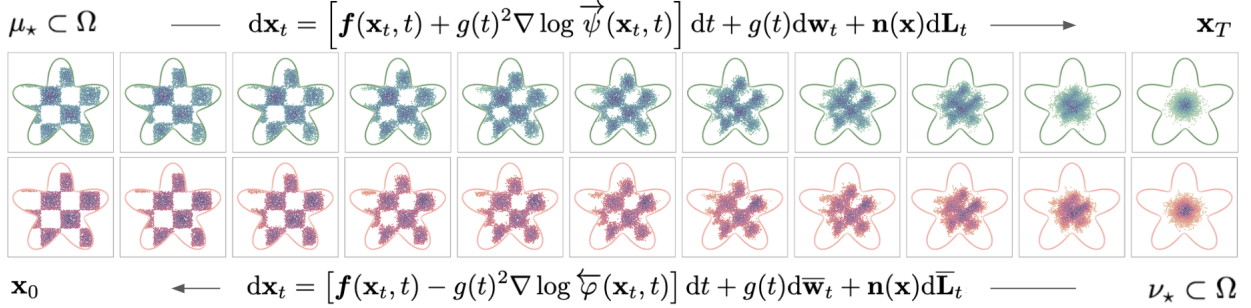


Figure 1: Constrained generative modeling via reflected forward-backward SDEs.

To bridge this gap, we propose the *Reflected Schrödinger Bridge* (SB) to model the transport between any smooth distributions with bounded support. We derive novel reflected forward-backward stochastic differential equations (reflected FB-SDEs) with Neumann and Robin boundary conditions and extend the divergence-based likelihood training to ensure its confinement within any smooth boundaries. We further establish connections between reflected FB-SDEs and EOT on bounded domains, where the latter facilitates the theoretical understanding by analyzing the convergence of the dual, potentials, and couplings on bounded domains. Notably, our analysis provides the first non-geometric approach to study the uniform-in-time stability w.r.t. the marginals and is noteworthy in its own right. We empirically validate our algorithm on 2D examples and standard image benchmarks, showcasing its promising performance in generative modeling over constrained domains. The flexible choices on the priors allow us to choose freely between VP-SDE and VE-SDE.

2 Related Works

Constrained Sampling Bubeck et al. [2018] studied the convergence of Langevin Monte Carlo within bounded domains. His work revealed a polynomial sample time for log-concave distributions, which is later extended to non-convex settings by Lamperski [2021]. Furthermore, the exploration of constrained sampling in challenging scenarios with ill-conditioned and non-smooth distributions was explored by Kook et al. [2022], who leveraged Hamiltonian Monte Carlo techniques. Other constrained sampling works include proximal Langevin dynamics [Brosse et al., 2017] and mirrored Langevin dynamics [Hsieh et al., 2018].

Constrained Generation De Bortoli et al. [2022], Huang et al. [2022] studied the extension of diffusion models on Riemannian manifolds, and the convergence is further analyzed by De Bortoli [2022]. This groundwork subsequently motivated follow-up research, including implicit score-matching loss via log-barrier methods and reflected Brownian motion [Fishman et al., 2023] and Schrödinger bridge [Thornton et al., 2022] on the Riemannian manifold. Alternatively, drawing inspiration from the popular thresholding technique in real-world diffusion applications, Lou and Ermon [2023] proposed to train explicit score-matching loss based on reflected Brownian motion, which demonstrated compelling empirical performance. Mirror diffusion models [Liu et al., 2023a] studied constrained generation on convex sets and found interesting applications in watermarked generations. Liu et al. [2023b] employed Doob’s h-transform to learn diffusion bridges on various constrained domains. The study of reflected Schrödinger bridge was initiated by Caluya and Halder [2021] in the control community and has shown remarkable performance in low-dimensional problems.

3 Preliminaries

Diffusion models [Song et al., 2021b] have achieved tremendous progress in real-world applications, such as image and text-to-image generation. However, real-world data (such as the bounded pixel space in images) often comes with

bounded support. As an illustration within the computer vision field, practitioners often employ ad-hoc thresholding techniques to project the data to the desired space, which inevitably affects the theoretical understanding and hinders future updates.

To generalize these techniques in a principled framework, [Lou and Ermon \[2023\]](#) utilized reflected Brownian motion to train explicit score-matching loss in bounded domains. They first perturb the data with a sequence of noise and then propose to generate the constrained data distribution through the corresponding reflected backward process [[Williams, 1987](#), [Cattiaux, 1988](#)].

$$d\mathbf{x}_t = \mathbf{f}(\mathbf{x}_t, t)dt + g(t)d\mathbf{w}_t + d\mathbf{L}_t, \quad \mathbf{x}_0 \sim p_{\text{data}} \subset \Omega \quad (1a)$$

$$d\mathbf{x}_t = [\mathbf{f}(\mathbf{x}_t, t) - g(t)^2 \nabla \log p_t(\mathbf{x}_t)] dt + g(t)d\bar{\mathbf{w}}_t + d\bar{\mathbf{L}}_t, \quad \mathbf{x}_T \sim p_{\text{prior}} \subset \Omega \quad (1b)$$

where Ω is the state space in \mathbb{R}^d ; $\mathbf{f}(\mathbf{x}_t, t)$ and $g(t)$ are the vector field and the diffusion term, respectively; \mathbf{w}_t is the Brownian motion; $\bar{\mathbf{w}}_t$ is another independent Brownian motion from time T to 0 ; \mathbf{L}_t and $\bar{\mathbf{L}}_t$ are the local time to confine the particle within the domain and are defined in Eq.(18); the marginal density at time t for the forward process (1a) is denoted by p_t . $\nabla \log p_t(\cdot)$ is the score function at time t , which is often approximated by a neural network model $s_\theta(\cdot, t)$. Given proper score approximations, the data distribution p_{data} can be generated from the backward process (1b).

4 Reflected Schrödinger bridge

Although reflected diffusion models have demonstrated empirical success in image applications on hypercubes, extensions to general domains with optimal-transport guarantee remain limited [[Lavenant and Santambrogio, 2022](#)]. Notably, the forward process (1a) requires a long time T to approach the prior distribution, which inevitably leads to a slow inference [[De Bortoli et al., 2021](#)]. To solve that problem, the dynamic SB problem on a bounded domain Ω proposes to solve

$$\inf_{\mathbb{P} \in \mathcal{D}(\mu_*, \nu_*)} \text{KL}(\mathbb{P} \parallel \mathbb{Q}), \quad (2)$$

where the coupling \mathbb{P} belongs to the path space $\mathcal{D}(\mu_*, \nu_*) \subset C(\Omega, [0, T])$ with marginal measures μ_* at time $t = 0$ and ν_* at $t = T$; \mathbb{Q} is the prior path measure, such as the measure induced by the path of the reflected Brownian motion or Ornstein-Uhlenbeck (OU) process. From the perspective of stochastic control, the dynamical SBP aims to minimize the cost along the reflected process

$$\begin{aligned} & \inf_{\mathbf{u} \in \mathcal{U}} \mathbb{E} \left\{ \int_0^T \frac{1}{2} \|\mathbf{u}(\mathbf{x}_t, t)\|_2^2 dt \right\} \\ \text{s.t. } & d\mathbf{x}_t = [\mathbf{f}(\mathbf{x}_t, t) + g(t)\mathbf{u}(\mathbf{x}_t, t)] dt + \sqrt{2\varepsilon}g(t)d\mathbf{w}_t + \mathbf{n}(\mathbf{x}_t)d\mathbf{L}_t, \\ & \mathbf{x}_0 \sim \mu_*, \quad \mathbf{x}_T \sim \nu_*, \quad \mathbf{x}_t \in \Omega, \quad \text{for any } t \in [0, T] \end{aligned} \quad (3)$$

where \mathcal{U} is a set of control functions; ε is the entropic regularizer for EOT; $\mathbf{n}(\mathbf{x})$ is an inner unit normal vector at $\mathbf{x} \in \partial\Omega$ and $\mathbf{0}$ for $\mathbf{x} \in \Omega$; the expectation follows from the density $\rho(\mathbf{x}, t)$. Simulation demos of the reflected SDEs are shown in Figure 2.

To derive the reflected FB-SDEs and training scheme, we first present standard assumptions on the regularity properties [[Øksendal, 2003](#)], as well as the smoothness of measure [[Chen et al., 2022a,b](#)] and boundary [[Lamperski, 2021](#)]:

Assumption A1 (Regularity on drift and diffusion). *The drift \mathbf{f} and diffusion term $g > 0$ satisfy the Lipschitz and linear growth condition.*

Assumption A2 (Smooth boundary). *The domain Ω is bounded and has a smooth boundary.*

Extensions to general convex domains (with corners) are also studied in [Lamperski \[2021\]](#).

Assumption A3 (Smooth measure). *The probability measures μ_* and ν_* are smooth in the sense that the energy functions $U_* = -\nabla \log \frac{d\mu_*}{d\mathbf{x}}$ and $V_* = -\nabla \log \frac{d\nu_*}{d\mathbf{x}}$ are differentiable.*

4.1 Reflected forward-backward stochastic differential equations

Following the tradition in mechanics [[Pavliotis, 2014](#)], we rewrite the reflected SBP as follows

$$\begin{aligned} & \inf_{\mathbf{u} \in \mathcal{U}} \int_0^T \int_{\Omega} \frac{1}{2} \rho \|\mathbf{u}\|_2^2 d\mathbf{x} dt \\ \text{s.t. } & \frac{\partial \rho}{\partial t} + \nabla \cdot \mathbf{J}|_{\mathbf{x} \in \Omega} = 0, \quad \langle \mathbf{J}, \mathbf{n} \rangle|_{\mathbf{x} \in \partial\Omega} = 0, \end{aligned} \quad (4)$$

where \mathbf{J} is the probability flux of continuity equation $\mathbf{J} \equiv \rho(\mathbf{f} + g\mathbf{u}) - \varepsilon g^2 \nabla \rho$ [Pavliotis, 2014].

We next solve the objectives with a Lagrangian multiplier: $\phi(\mathbf{x}, t)$. Applying the Stokes theorem with details presented in appendix 8.1, we have

$$\mathcal{L}(\rho, \mathbf{u}, \phi) = \underbrace{\int_0^T \int_{\Omega} \left(\frac{1}{2} \rho \|\mathbf{u}\|_2^2 - \rho \frac{\partial \phi}{\partial t} - \langle \nabla \phi, \mathbf{J} \rangle \right) d\mathbf{x} dt}_{\bar{\mathcal{L}}(\rho, \mathbf{u}, \phi)} + \underbrace{\int_{\Omega} \phi \rho|_{t=0} d\mathbf{x}}_{\text{constant term w.r.t. } \mathbf{u}} + \underbrace{\int_0^T \int_{\partial\Omega} \langle \mathbf{J}, \mathbf{n} \rangle d\sigma(\mathbf{x}) dt}_{:=0 \text{ by Eq.(4)}}$$

Minimizing \mathcal{L} with respect to \mathbf{u} , we can obtain $\mathbf{u}^* = g \nabla \phi$. Further applying the Cole-Hopf transform $\vec{\psi}(\mathbf{x}, t) = \exp\left(\frac{\phi(\mathbf{x}, t)}{2\varepsilon}\right)$ and setting $\bar{\mathcal{L}}(\rho, \mathbf{u}^*, \phi) = 0$, we derive the *backward Kolmogorov equation* with *Neumann boundary conditions*

$$\begin{cases} \frac{\partial \vec{\psi}}{\partial t} + \varepsilon g^2 \Delta \vec{\psi} + \langle \nabla \vec{\psi}, \mathbf{f} \rangle = 0 & \text{in } \Omega \\ \langle \nabla \vec{\psi}, \mathbf{n} \rangle = 0 & \text{on } \partial\Omega. \end{cases}$$

Next we define $\overleftarrow{\varphi} = \rho^* / \vec{\psi}$, where ρ^* is the optimal density of Eq.(3) given \mathbf{u}^* . We arrive at the *forward Kolmogorov equation* with the *Robin boundary condition*

$$\begin{cases} \partial_t \overleftarrow{\varphi} + \nabla \cdot (\overleftarrow{\varphi} \mathbf{f} - \varepsilon g^2 \nabla \overleftarrow{\varphi}) = 0 & \text{in } \Omega \\ \langle \overleftarrow{\varphi} \mathbf{f} - \varepsilon g^2 \nabla \overleftarrow{\varphi}, \mathbf{n} \rangle = 0 & \text{on } \partial\Omega. \end{cases}$$

Despite the elegance, solving PDEs in high dimensions often poses significant challenges due to the curse of dimensionality [Han et al., 2019]. To overcome these challenges, we resort to presenting a set of reflected FB-SDEs:

Theorem 1. Consider a Schrödinger (PDE) system with Neumann and Robin boundary conditions

$$\begin{cases} \frac{\partial \vec{\psi}}{\partial t} + \langle \nabla \vec{\psi}, \mathbf{f} \rangle + \varepsilon g^2 \Delta \vec{\psi} = 0 \\ \frac{\partial \overleftarrow{\varphi}}{\partial t} + \nabla \cdot (\overleftarrow{\varphi} \mathbf{f} - \varepsilon g^2 \nabla \overleftarrow{\varphi}) = 0 \end{cases} \quad \text{s.t. } \langle \nabla \vec{\psi}, \mathbf{n} \rangle|_{\mathbf{x} \in \partial\Omega} = 0, \langle \mathbf{f} \overleftarrow{\varphi} - \varepsilon g^2 \nabla \overleftarrow{\varphi}, \mathbf{n} \rangle|_{\mathbf{x} \in \partial\Omega} = 0. \quad (5)$$

Solving the PDE system gives rise to the reflected FB-SDEs with $\mathbf{x}_t \in \Omega$

$$d\mathbf{x}_t = \left[\mathbf{f}(\mathbf{x}_t, t) + 2\varepsilon g(t)^2 \nabla \log \vec{\psi}(\mathbf{x}_t, t) \right] dt + \sqrt{2\varepsilon} g(t) d\mathbf{w}_t + \mathbf{n}(\mathbf{x}) d\mathbf{L}_t, \quad \mathbf{x}_0 \sim \mu_*, \quad (6a)$$

$$d\mathbf{x}_t = \left[\mathbf{f}(\mathbf{x}_t, t) - 2\varepsilon g(t)^2 \nabla \log \overleftarrow{\varphi}(\mathbf{x}_t, t) \right] dt + \sqrt{2\varepsilon} g(t) d\bar{\mathbf{w}}_t + \mathbf{n}(\mathbf{x}) d\bar{\mathbf{L}}_t, \quad \mathbf{x}_T \sim \nu_*. \quad (6b)$$

The connection to the probability flow ODE is also studied and presented in section 8.2.

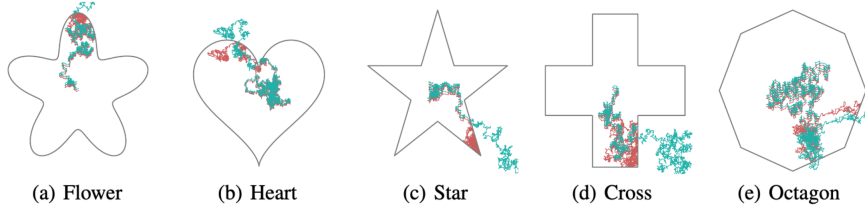


Figure 2: Reflected OU processes (reflected v.s. unconstrained), driven by the same Brownian motion, excluding the reflections. All boundary curves have properly defined unit vectors.

4.2 Likelihood training

It is worth mentioning that the reflected FB-SDE (6) is not directly accessible due to the unknown control variables $(\nabla \log \vec{\psi}, \nabla \log \overleftarrow{\varphi})$. To tackle this issue, a standard tool is the (nonlinear) Feynman-Kac formula [Ma and Yong, 2007, Karatzas and Shreve, 1998], which leads to a stochastic representation.

Proposition 1 (Feynman-Kac representation). Assume assumptions A1-A2 hold. $\overleftarrow{\varphi}$ satisfies a PDE (5) and \mathbf{x}_t follows from a diffusion (6a). Define $\vec{y}_t \equiv \vec{y}(\mathbf{x}_t, t) = \log \vec{\psi}(\mathbf{x}_t, t)$ and $\overleftarrow{y}_t \equiv \overleftarrow{y}(\mathbf{x}_t, t) = \log \overleftarrow{\varphi}(\mathbf{x}_t, t)$. Then \overleftarrow{y}_s admits a stochastic representation

$$\overleftarrow{y}_s = \mathbb{E} \left[\overleftarrow{y}_T - \underbrace{\int_s^T \left(\frac{1}{2} \|\overleftarrow{\mathbf{z}}_t\|_2^2 + \nabla \cdot (\overleftarrow{g} \mathbf{z}_t - \mathbf{f}) + \langle \overleftarrow{\mathbf{z}}_t, \overleftarrow{\mathbf{z}}_t \rangle \right) dt}_{\zeta(\mathbf{x}_t, t)} - d\overleftarrow{\mathbf{L}}_t \middle| \mathbf{x}_s = \mathbf{x}_s \right],$$

on $\Omega \times [0, T]$; $\overleftarrow{\mathbf{z}}_t \equiv \overleftarrow{\mathbf{z}}(\mathbf{x}_t, t) = g \nabla \overleftarrow{y}_t$, $\overleftarrow{\mathbf{z}}_t \equiv \overleftarrow{\mathbf{z}}(\mathbf{x}_t, t) = g \nabla \overleftarrow{y}_t$, $d\overleftarrow{\mathbf{L}}_t = \frac{1}{g} \langle \overleftarrow{\mathbf{z}}_t, \mathbf{n}_t \rangle d\mathbf{L}_t$.

Sketch of proof The proof primarily relies on Theorem 3 from Chen et al. [2022b] and applies (generalized) Itô's lemma to \overleftarrow{y}_t using (5) and (6a). The difference is to incorporate the generalized Itô's lemma [Bubeck et al., 2018, Lamperski, 2021] to address the local time of \mathbf{x}_t at the boundary $\partial\Omega$. Subsequently, our analysis establishes that $\overleftarrow{y}_s - \int_{s_1}^s \zeta(\mathbf{x}_t, t)$, where $s \in [s_1, T]$, is a martingale within the domain Ω , which concludes our proposition. \square

A direct application of the proposition is to obtain the log-likelihood \overleftarrow{y}_0 given data points \mathbf{x}_0 . With parametrized models $(\overrightarrow{\mathbf{z}}_t^\theta, \overleftarrow{\mathbf{z}}_t^\omega)$ to approximate $(\overrightarrow{\mathbf{z}}_t, \overleftarrow{\mathbf{z}}_t)$, we can optimize the backward score function $\overleftarrow{\mathbf{z}}_t^\omega$ through the forward loss function $\mathcal{L}(\mathbf{x}_0; \omega)$ in Algorithm 1. Regarding the forward-score estimation, similar to Theorem 11 [Chen et al., 2022b], the symmetric property of the reflected SB also enables to optimize $\overrightarrow{\mathbf{z}}_t$ via the backward loss function $\mathcal{L}(\mathbf{x}_T; \theta)$.

Algorithm 1 One iteration of the backward-forward score function solver to optimize $(\overrightarrow{\mathbf{z}}_t^\theta, \overleftarrow{\mathbf{z}}_t^\omega)$ with the reflection implemented in Algorithm 4. We cache the trajectories following De Bortoli et al. [2021] to avoid expensive computational graphs. In practice, $\mathbb{E}[\log \overleftarrow{y}_T]$ and $\mathbb{E}[\log \overrightarrow{y}_0]$ are often omitted to facilitate training [Chen et al., 2022b].

$$\begin{aligned} \mathcal{L}(\mathbf{x}_0; \omega) &= - \int_0^T \mathbb{E}_{\mathbf{x}_t \sim (6a)} \left[\left(\frac{1}{2} \|\overleftarrow{\mathbf{z}}_t^\omega\|_2^2 + g \nabla \cdot \overleftarrow{\mathbf{z}}_t^\omega + \langle \overrightarrow{\mathbf{z}}_t^\theta, \overleftarrow{\mathbf{z}}_t^\omega \rangle \right) dt + d\overleftarrow{\mathbf{L}}_t^\omega \Big| \mathbf{x}_0 = \mathbf{x}_0 \right] \\ \mathcal{L}(\mathbf{x}_T; \theta) &= - \int_0^T \mathbb{E}_{\mathbf{x}_t \sim (6b)} \left[\left(\frac{1}{2} \|\overrightarrow{\mathbf{z}}_t^\theta\|_2^2 + g \nabla \cdot \overrightarrow{\mathbf{z}}_t^\theta + \langle \overleftarrow{\mathbf{z}}_t^\omega, \overrightarrow{\mathbf{z}}_t^\theta \rangle \right) dt + d\overrightarrow{\mathbf{L}}_t^\theta \Big| \mathbf{x}_T = \mathbf{x}_T \right], \end{aligned}$$

where $d\overleftarrow{\mathbf{L}}_t^\omega = \frac{1}{g} \langle \overleftarrow{\mathbf{z}}_t^\omega, \mathbf{n}_t \rangle d\mathbf{L}_t$ and $d\overrightarrow{\mathbf{L}}_t^\theta = \frac{1}{g} \langle \overrightarrow{\mathbf{z}}_t^\theta, \mathbf{n}_t \rangle d\overline{\mathbf{L}}_t$. (6a) (respectively, (6b)) is approximated via $\overrightarrow{\mathbf{z}}_t^\theta$ (respectively, $\overleftarrow{\mathbf{z}}_t^\omega$).

By the data processing inequality, our loss function provides a lower bound of the log-likelihood, which resembles the evidence lower bound (ELBO) in variational inference [Song et al., 2021a]. We can expect a smaller variational gap given more accurate parametrized models.

When the domain is taken to be $\Omega = \mathbb{R}^d$, the aforementioned solvers become equivalent to the loss function (18-19) presented in Chen et al. [2022b].

4.3 Connections to the IPF algorithm

Similar in spirit to Theorem 3 of Song et al. [2021a], Algorithm 1 results in an elegant half-bridge solver ($\mu_\star \rightarrow \nu_\star$ v.s. $\mu_\star \leftarrow \nu_\star$) to approximate the primal formulation [Nutz, 2022] of the dynamic Schrödinger bridge (2) [De Bortoli et al., 2021, Vargas et al., 2021]:

$$\text{Dynamic Primal IPF} \quad \mathbb{P}_{2k} = \arg \min_{\mathbb{P} \in \mathcal{D}(\cdot, \nu_\star)} \text{KL}(\mathbb{P} \| \mathbb{P}_{2k-1}), \quad \mathbb{P}_{2k+1} = \arg \min_{\mathbb{P} \in \mathcal{D}(\mu_\star, \cdot)} \text{KL}(\mathbb{P} \| \mathbb{P}_{2k}), \quad (7)$$

which is also known as the dynamic IPF algorithm (also known as Sinkhorn algorithm) [Ruschendorf, 1995, De Bortoli et al., 2021]. Consider the disintegration of the path measure $\mathbb{P} = \pi \otimes \mathbb{P}^{\mu_\star, \nu_\star}$

$$\mathbb{P}(\cdot) = \iint_{\Omega^2} \mathbb{P}^{\mathbf{x}_0, \mathbf{x}_T}(\cdot) \pi(d\mathbf{x}_0, d\mathbf{x}_T), \quad (8)$$

where $\mathbb{P}^{\mathbf{x}_0, \mathbf{x}_T} \in \mathbb{P}^{\mu_\star, \nu_\star}$ is a diffusion bridge from $\mathbf{x}_0 = \mathbf{x}_0$ to $\mathbf{x}_T = \mathbf{x}_T$, $\pi \in \Pi(\mu_\star, \nu_\star)$ and the product space $\Pi(\mu_\star, \nu_\star) \subset \Omega^2$ denotes the space of couplings with the first and second marginals following from μ_\star and ν_\star , respectively. Now project the path space \mathcal{D} to the product space Π . We have the static IPF algorithm in the primal formulation:

$$\text{Static Primal IPF} \quad \pi_{2k} = \arg \min_{\pi \in \Pi(\cdot, \nu_\star)} \text{KL}(\pi \| \pi_{2k-1}), \quad \pi_{2k+1} = \arg \min_{\pi \in \Pi(\mu_\star, \cdot)} \text{KL}(\pi \| \pi_{2k}). \quad (9)$$

5 Convergence analysis via entropic optimal transport

The dynamic IPF algorithm offers an efficient training scheme to fit marginals in high-dimensional problems. However, the understanding of the convergence remains unclear to the machine learning community. To get around this issue, we leverage the progress from the static optimal transport on bounded domains and costs [Carlier, 2022, Chen et al., 2016, Deligiannidis et al., 2021].

Our analysis is illustrated as follows: We first draw connections between dynamic and static (primal) IPFs by projecting the path space \mathcal{D} to the product space Π and then show the equivalence between the dual and primal formulations. Next, we perturb the marginals (in terms of energy functions) and show the approximate linear convergence of the dual, potential, and then static couplings. The convergence of dynamic couplings can be expected given a reasonable estimate of diffusion bridge.

$$\text{Dynamic Primal IPF (7)} \xleftrightarrow[\text{Projection}]{\text{Disintegration}} \text{Static Primal IPF (9)} \xleftrightarrow[\text{Lemma 1}]{\text{Equivalence(9.5)}} \text{Static Dual IPF (13)}$$

5.1 Equivalence between Dynamic SBP and Static SBP

Assuming the solutions exist, the disintegration of measures implies that the equivalence of solutions between the dynamic and static SBPs [Léonard, 2014]:

$$\text{Dynamic SBP} \quad \mathbb{P}_* = \arg \min_{\mathbb{P} \in \mathcal{D}(\mu_*, \nu_*)} \text{KL}(\mathbb{P} \parallel \mathbb{Q}) \iff \pi_* = \arg \min_{\pi \in \Pi(\mu_*, \nu_*)} \text{KL}(\pi \parallel \mathcal{G}), \quad \text{Static}$$

where π (respectively, \mathcal{G}) is the projection of the path measure \mathbb{P} (respectively, \mathbb{Q}) on the product space at $t = 0$ and T ; $d\mathcal{G} \propto e^{-c_\varepsilon} d(\mu_* \otimes \nu_*)$; c_ε is a cost function. Both the dynamic and static SBP formulations yield structure properties (see the Born's formula in Léonard [2014]) and enables to represent Schrödinger bridges \mathbb{P}_* and π_* using Schrödinger potentials φ_* and ψ_* :

$$\text{Dynamic Structure} \quad d\mathbb{P}_* = e^{\varphi_*(\mathbf{x}) + \psi_*(\mathbf{y})} d\mathbb{Q} \iff d\pi_*(\mathbf{x}, \mathbf{y}) = e^{\varphi_*(\mathbf{x}) + \psi_*(\mathbf{y})} d\mathcal{G}. \quad \text{Static} \quad (10)$$

Moreover, the summation $\varphi_* \oplus \psi_*$ is unique such that $(\varphi_* + a) \oplus (\psi_* - a)$ is also viable for any a .

This static structural representation establishes a connection between the static SBP and entropic optimal transport (EOT) with a unit entropy regularizer [Chen et al., 2023], and the latter results in an efficient scheme to compute the optimal coupling:

$$\inf_{\pi \in \Pi(\mu_*, \nu_*)} \iint_{\Omega^2} c_\varepsilon(\mathbf{x}, \mathbf{y}) \pi(d\mathbf{x}, d\mathbf{y}) + \text{KL}(\pi \parallel \mu_* \otimes \nu_*).$$

5.2 Duality for Schrödinger bridges and Approximations

The Schrödinger bridge is a constrained optimization problem and possesses a computation-friendly dual formulation. Moreover, the duality gap is zero under probability measures [Léonard, 2001].

Lemma 1 (Duality [Nutz, 2022]). *Given assumptions A1-A3, the dual via potentials (φ, ψ) follows*

$$\min_{\pi \in \Pi(\mu_*, \nu_*)} \text{KL}(\pi \parallel \mathcal{G}) = \max_{\varphi, \psi} G(\varphi, \psi), \quad G(\varphi, \psi) := \mu_*(\varphi) + \nu_*(\psi) - \iint_{\Omega^2} e^{\varphi \oplus \psi} d\mathcal{G} + 1, \quad (11)$$

where $\mu_*(\varphi) = \int_{\Omega} \varphi d\mu_*$, $\nu_*(\psi) = \int_{\Omega} \psi d\nu_*$, $\varphi \in L^1(\mu_*)$, and $\psi \in L^1(\nu_*)$.

An effective solver is to maximize the dual G via $\varphi_{k+1} = \arg \max_{\varphi \in L^1(\mu_*)} G(\varphi, \psi_k)$ and $\psi_{k+1} = \arg \max_{\psi \in L^1(\nu_*)} G(\varphi_{k+1}, \psi)$ alternatingly. From a geometric perspective, alternating maximization corresponds to alternating projections (detailed in Appendix 9.4)

$$\varphi_{k+1} = \arg \max_{\varphi \in L^1(\mu_*)} G(\varphi, \psi_k) \implies \text{the first marginal of } \pi(\varphi_{k+1}, \psi_k) \text{ is } \mu_*, \quad (12a)$$

$$\psi_{k+1} = \arg \max_{\psi \in L^1(\nu_*)} G(\varphi_{k+1}, \psi) \implies \text{the second marginal of } \pi(\varphi_{k+1}, \psi_{k+1}) \text{ is } \nu_*. \quad (12b)$$

The marginal properties of the coupling implies the Schrödinger equation [Nutz and Wiesel, 2022]

$$\varphi_*(\mathbf{x}) = -\log \int_{\Omega} e^{\psi_*(\mathbf{y}) - c_\varepsilon(\mathbf{x}, \mathbf{y})} \nu_*(d\mathbf{y}), \quad \psi_*(\mathbf{y}) = -\log \int_{\Omega} e^{\varphi_*(\mathbf{x}) - c_\varepsilon(\mathbf{x}, \mathbf{y})} \mu_*(d\mathbf{x}).$$

Since the Schrödinger potential functions (ψ_*, φ_*) are not known *a priori*, the dual formulation of the static IPF algorithm was proposed to solve the alternating projections as follows:

$$\text{Static Dual IPF : } \psi_k(\mathbf{y}) = -\log \int_{\Omega} e^{\varphi_k(\mathbf{x}) - c_\varepsilon(\mathbf{x}, \mathbf{y})} \mu_*(d\mathbf{x}), \quad \varphi_{k+1}(\mathbf{x}) = -\log \int_{\Omega} e^{\psi_k(\mathbf{y}) - c_\varepsilon(\mathbf{x}, \mathbf{y})} \nu_*(d\mathbf{y}). \quad (13)$$

The equivalence between the primal IPF and dual IPF is further illustrated in Appendix 9.5.

However, given a limited computational budget, projecting to the ideal measure μ_* (or ν_*) in Eq.(12) at each iteration may not be practical. Instead, some close approximation $\mu_{*,k+1}$ (or $\nu_{*,k}$) is used at iteration $2k+1$ (or $2k$) via Gaussian processes [Vargas et al., 2021] or neural networks [De Bortoli et al., 2021, Chen et al., 2022b]. Therefore, one may resort to an approximate marginal that still achieves reasonable accuracy:

$$\mu_{2k+1} = \mu_{*,k+1} \approx \mu_*, \quad \nu_{2k} = \nu_{*,k} \approx \nu_*. \quad (14)$$

We refer to the IPF algorithm with approximate marginals as approximate IPF (aIPF) and present the static dual formulation of aIPF in Algorithm 2. The difference between IPF and aIPF is detailed in Figure 3. The structure representation (10) can be naturally extended based on approximate marginals and is also studied by Deligiannidis et al. [2021]

$$\begin{aligned} d\pi_{2k} &= e^{\varphi_k \oplus \psi_k - c_\varepsilon} d(\mu_{*,k} \otimes \nu_{*,k}), \\ d\pi_{2k-1} &= e^{\varphi_k \oplus \psi_{k-1} - c_\varepsilon} d(\mu_{*,k} \otimes \nu_{*,k-1}), \end{aligned} \quad (15)$$

where π_k is the approximate coupling at iteration k . By the structural properties in Eq.(10), the representation also applies to the dynamic settings, which involves the computation of the static IPF, followed by its integration with a diffusion bridge [Eckstein and Nutz, 2022].

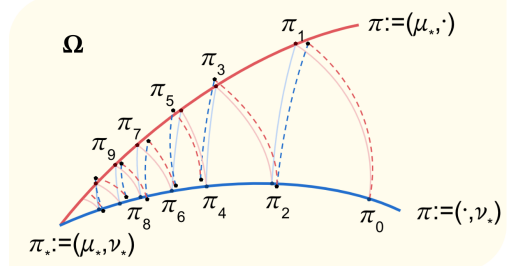


Figure 3: IPF v.s. aIPF. The approximate (or exact) projections are highlighted through the dotted (or solid) lines.

Algorithm 2 One iteration of aIPF (static). The static coupling π_k can be recovered by the structural representation in (15); the dynamic coupling $\mathbb{P}_k = \iint_{\Omega^2} \mathbb{P}_k^{\mathbf{x}_0, \mathbf{x}_T}(\cdot) \pi_k(\mathbf{x}_0, \mathbf{x}_T)$ can be solved by further learning a diffusion bridge $\mathbb{P}_k^{\mathbf{x}_0, \mathbf{x}_T}$.

$$\psi_k(\mathbf{y}) = -\log \int_{\Omega} e^{\varphi_k(\mathbf{x}) - c_\varepsilon(\mathbf{x}, \mathbf{y})} \mu_{*,k}(d\mathbf{x}), \quad \varphi_{k+1}(\mathbf{x}) = -\log \int_{\Omega} e^{\psi_k(\mathbf{y}) - c_\varepsilon(\mathbf{x}, \mathbf{y})} \nu_{*,k}(d\mathbf{y}). \quad (16)$$

5.3 Convergence of Couplings with bounded domain

Despite the rich literature on the analysis of SBP within bounded domains [Chen et al., 2016], most of them are not applicable to practical scenarios where exact marginals are not available. To fill this gap, we extend the linear convergence analysis with perturbed marginals. The key to our proof is the strong convexity of the dual (11). To quantify the convergence, similar to De Bortoli [2022], we introduce an additional assumption to control the perturbation of the marginals in the sense that:

Assumption A4 (Marginal perturbation). $U_k = \nabla \log \frac{d\mu_{*,k}}{d\mathbf{x}}$ and $V_k = \nabla \log \frac{d\nu_{*,k}}{d\mathbf{x}}$ are the approximate energy functions at the k -th iteration and are ϵ -close to energy functions U_* and V_*

$$\|U_k(\mathbf{x}) - U_*(\mathbf{x})\|_2 \leq \epsilon(1 + \|\mathbf{x}\|_2), \quad \|V_k(\mathbf{x}) - V_*(\mathbf{x})\|_2 \leq \epsilon(1 + \|\mathbf{x}\|_2), \quad \forall \mathbf{x} \in \Omega.$$

Note that the Lipschitz cost function on Ω^2 is also a standard assumption [Deligiannidis et al., 2021]. It is not required here by Assumption A1, which leads to a smooth transition kernel and cost function.

Recall the connections between dynamic primal IPF and static dual IPF, we know ϵ mainly depends on the score-function $(\vec{\mathbf{z}}_t^\theta, \overleftarrow{\mathbf{z}}_t^\omega)$ estimations [Song et al., 2021a] and numerical discretizations. More concrete connections between them will be left as future work. In addition, the errors in the two marginals don't have to be the same, and we use a unified ϵ mainly for analytical convenience.

Moreover, we use the same domain Ω for both marginals to be consistent with our algorithm in Section 4. The proof can be easily extended to different domains X and Y for μ_* and ν_* .

Approximately linear convergence and proof sketches We first follow Carlier [2022], Nutz [2022], Marino and Gerolin [2020] to build a *centered* aIPF algorithm in Algorithm 3 with scaled potential functions $\bar{\varphi}_k$ and $\bar{\psi}_k$ such that $\mu_*(\bar{\varphi}_k) = 0$. Since the summations of the potentials φ_* and ψ_* are unique by (10), the *centering* operation doesn't change the dual objective but ensures that the aIPF iterates are uniformly bounded in Lemma 4 with the help of the decomposition

$$\|\bar{\varphi} \oplus \bar{\psi}\|_{L^2(\mu_* \otimes \nu_*)}^2 = \|\bar{\varphi}\|_{L^2(\mu_*)}^2 + \|\bar{\psi}\|_{L^2(\nu_*)}^2 \quad \text{if } \mu_*(\bar{\varphi}) = 0.$$

How to ensure centering with perturbed marginals in Algorithm 3 is crucial and one major novelty in our proof. We next exploit the *strong convexity* of the exponential function e^x associated with the concave dual. We obtain an auxiliary result regarding the convergence of the dual and the potentials.

Lemma 2 (Convergence of the Dual and Potentials). *Let $(\bar{\varphi}_k, \bar{\psi}_k)_{k \geq 0}$ be the iterates of a variant of Algorithm 2. Given assumptions A1-A4 with small enough marginal perturbations ϵ , we have*

$$\begin{aligned} G(\bar{\varphi}_\star, \bar{\psi}_\star) - G(\bar{\varphi}_k, \bar{\psi}_k) &\lesssim (1 - e^{-24\|c_\epsilon\|_\infty})^k + e^{24\|c_\epsilon\|_\infty} \epsilon, \\ \|\bar{\varphi}_\star - \bar{\varphi}_k\|_{L^2(\mu_\star)} + \|\bar{\psi}_\star - \bar{\psi}_k\|_{L^2(\nu_\star)} &\lesssim e^{3\|c_\epsilon\|_\infty} (1 - e^{-24\|c_\epsilon\|_\infty})^{k/2} + e^{15\|c_\epsilon\|_\infty} \epsilon^{1/2}. \end{aligned}$$

Since the centering operation doesn't change the structure property (10), we are able to analyze the convergence of the static couplings. Motivated by Theorem 3 of Deligiannidis et al. [2021], we exploit the structural property (10) to estimate the \mathbf{W}_1 distance based on its dual formulation.

Theorem 2 (Convergence of Static Couplings). *Given assumptions A1-A4 with small marginal perturbations ϵ , the iterates of the couplings $(\pi_k)_{k \geq 0}$ in Algorithm 2 satisfy the following result*

$$\mathbf{W}_1(\pi_k, \pi_\star) \leq O(e^{9\|c_\epsilon\|_\infty} (1 - e^{-24\|c_\epsilon\|_\infty})^{k/2} + e^{21\|c_\epsilon\|_\infty} \epsilon^{1/2}).$$

Such a result provides the worst-case guarantee on the convergence of the static couplings π_k . For example, to obtain a ϵ_\star - \mathbf{W}_1 distance, we can run $\Omega(e^{24\|c_\epsilon\|_\infty} (\|c_\epsilon\|_\infty - \log(\epsilon_\star \wedge 1)))$ iterations to achieve the goal. Recall that $c_\epsilon = c/\epsilon$ [Chen et al., 2023], a large entropic-regularizer ϵ may be needed in practice to yield reasonable performance, which also leads to specific tuning guidance on ϵ .

Our proof employs a non-geometric method to show the uniform in time stability, w.r.t. the marginals. Unlike the elegant approach [Deligiannidis et al., 2021] based on the Hilbert-Birkhoff projective metric [Chen et al., 2016], ours does not require advanced tools and may be more friendly to readers.

Recall the bridge representation in Eq.(8), we have $\mathbf{W}_1(\pi_k \otimes \mathbb{P}_k^{\mu_\star, \nu_\star}, \pi_\star \otimes \mathbb{P}_\star^{\mu_\star, \nu_\star}) \leq \mathbf{W}_1(\pi_k, \pi_\star) + \mathbf{W}_1(\mathbb{P}_k^{\mu_\star, \nu_\star}, \mathbb{P}_\star^{\mu_\star, \nu_\star})$. Assume the same assumptions as in Theorem 2, we arrive at the final result:

Proposition 2 (Convergence of Dynamic Couplings). *The iterates of the dynamic couplings $(\mathbb{P}_k)_{k \geq 0}$ in Algorithm 1 satisfy the following result*

$$\mathbf{W}_1(\mathbb{P}_k, \mathbb{P}_\star) \leq O(e^{9\|c_\epsilon\|_\infty} (1 - e^{-24\|c_\epsilon\|_\infty})^{k/2} + e^{21\|c_\epsilon\|_\infty} \epsilon^{1/2}) + \mathbf{W}_1(\mathbb{P}_k^{\mu_\star, \nu_\star}, \mathbb{P}_\star^{\mu_\star, \nu_\star}).$$

The result paves the way for understanding the general convergence of the dynamic IPF algorithm by incorporating a proper approximation of the diffusion bridge [Heng et al., 2022].

6 Empirical Simulations

6.1 Generation of 2D synthetic data

We first employ the reflected SB algorithm to generate three synthetic examples: checkerboard and Gaussian mixtures from a Gaussian prior and spiral from a moon prior. The domains are defined to be flower, octagon, and heart, where all boundary points are defined to have proper unit-vectors. We follow Chen et al. [2022b] and adopt a U-net to model $(\vec{\mathbf{z}}_t^\theta, \overleftarrow{\mathbf{z}}_t^\omega)$. We chose RVP-SDE as the base simulator from time 0 to $T = 1$, where the dynamics are discretized into 100 steps.

Our generated examples are presented in Figure 1 and 4. We see that all the data are generated smoothly from the prior and the forward and backward process matches with each other elegantly. To the best of our knowledge, this is the first algorithm (with OT guarantees) that works on custom domains. Other related work, such as Lou and Ermon [2023], mainly focuses on hypercubes in computer vision. We also visualize the forward-backward policies $\overleftarrow{\mathbf{z}}_t^\omega$ and $\vec{\mathbf{z}}_t^\theta$ in Figure 4. Our observations reveal that the forward vector fields $\vec{\mathbf{z}}_t^\theta$ demonstrate substantial nonlinearity when compared to the linear forward policy in SGMs, and furthermore, the forward vector fields exhibit pronounced dissimilarity when compared to the backward vector fields $\overleftarrow{\mathbf{z}}_t^\omega$.

6.2 Generation of Image Data

We test our method on large-scale image datasets using CIFAR-10 and ImageNet 64×64 . As the RGB value is between $[0, 1]$, we naturally select the domain as $\Omega = [0, 1]^d$, where $d = 3 \times 32 \times 32$ for the CIFAR-10 task and $d = 3 \times 64 \times 64$ for the ImageNet task. It is known that the SB system can be initialized with score-based generative models [Chen et al.,

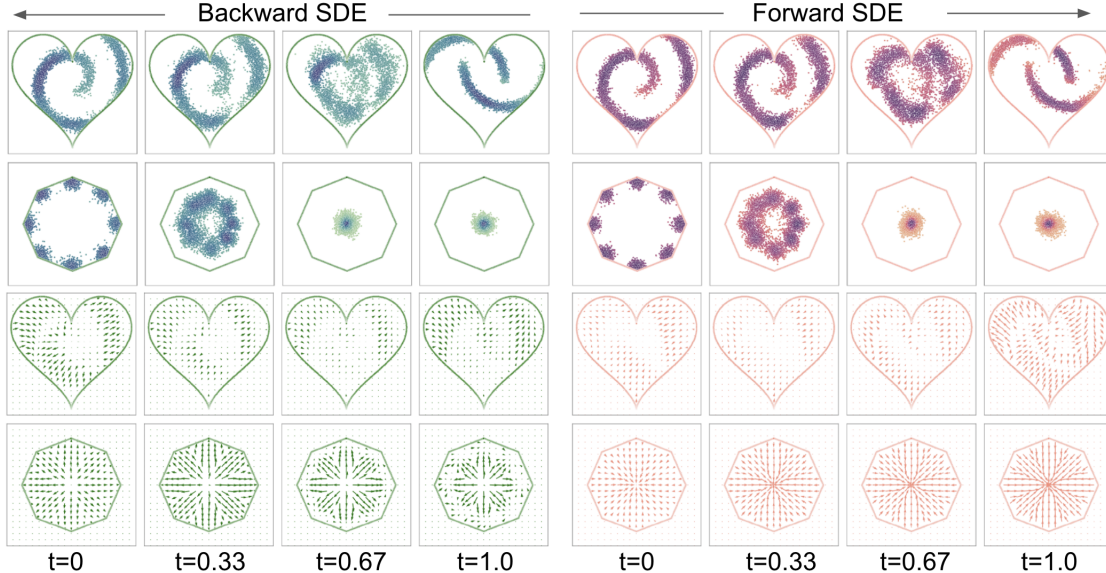


Figure 4: Demo of generative samples (top) and vector fields (bottom) based on Reflected SB.

2022b] and the warm-up study for reflected SB is presented in Appendix 10.2. We choose RVE-SDE as the prior path measure. The prior distribution of ν_* is the uniform distribution on Ω . The SDE is discretized into 1000 steps. In both scenarios, images are generated unconditionally, and the quality of the samples is evaluated using Frechet Inception Distance (FID) over 50,000 samples. The forward score function is modeled using U-net structure; the backward score function uses NCSN++ [Song et al., 2021b] for the CIFAR-10 task and ADM [Dhariwal and Nichol, 2022] for the ImageNet task. Details of the experiments are shown in Appendix 10.

We have included baselines for both constrained and unconstrained generative models and summarized the experimental results in Table 1. While our model may not surpass the state-of-the-art models, the minor improvement over the unconstrained SB-FBSDE [Chen et al., 2022b] underscores the effectiveness of the reflection operation. Moreover, the experiments verify the scalability of the reflected model and the training process is consistent with the findings in Lou and Ermon [2023], where the reflection in cube domains is easy to implement and the generation becomes more stable. Sample outputs are showcased in Figure 5 (including MNIST), with additional figures available in Appendix 10. Notably, our generated samples exhibit diversity and are visually indistinguishable from real data.

CIFAR-10	Constrained	OT	NLL	FID
MCSN++ [Song et al., 2021b]	No	No	2.99	2.20
DDPM [Ho et al., 2020]	No	No	3.75	3.17
SB-FBSDE [Chen et al., 2022b]	No	Yes	-	3.01
Reflected SGM [Lou and Ermon, 2023]	Yes	No	2.68	2.72
Ours	Yes	Yes	3.08	2.98
ImageNet 64×64				
PGMGAN [Armandpour et al., 2021]	No	No	-	21.73
GLIDE [Li et al., 2023]	No	No	-	29.18
GRB [Park and Shin, 2022]	No	No	-	26.57
Ours	Yes	Yes	3.20	23.95

Table 1: Evaluation of generative models on image data.

6.3 Generation in the Simplex Domain

Alongside the irregular domains illustrated in Figure 2 and the hypercube for image generation, we implement the method on the high-dimensional *projected simplex*. A d -projected simplex is defined as $\Delta_d := \{\mathbf{x} \in \mathbb{R}^d : \sum_i \mathbf{x}_i \leq 1, \mathbf{x}_i \geq 0\}$. Our method relies on reflected diffusion process instead of using diffeomorphic mapping (stick breaking) as in Lou and Ermon [2023]. As a comparison, we replicate the generative process using diffeomorphic mapping as well.

The data is created by collecting the image classification scores of Inception v3 from the last softmax layer with 1008 dimension. All the data fit into the projected simplex Δ_{1008} . The Inception model is loaded from a pretrained checkpoint[†], and the classification task is performed on the 64 × 64 Imagenet validation dataset of 50,000 images. The neural network of the score function is composed of 6 dense layers with 512 latent nodes. In every diffusion step, we use the reflection operator described in Algorithm 4 to constrain the data within the projected simplex. The alternative

[†]https://github.com/mseitzer/pytorch-fid/releases/download/fid_weights



Figure 5: Samples via reflected SB on MNIST (left), CIFAR10 (middle), and ImageNet 64 (right).

method is using stick breaking method to constrain the diffusion process. The transformation includes the mapping $[f(\mathbf{x})]_i = x_i \prod_{j=i+1}^d (1 - x_j)$ and the inverse mapping $[f^{-1}(\mathbf{y})]_i = \frac{y_i}{1 - \sum_{j=i+1}^d y_j}$. In every diffusion step, it first maps the data into an unit cube domain using reflection, then uses the forward transformation to map it within the projected simplex.

The results are shown in Figure 6. We compare the generated distribution of the most likely classes. The category index is in the same order of the pre-trained model’s output. The last plot in Figure 6 compares the cumulative distribution of the ground truth and generated distribution, providing a cleaner view of the comparison. The curve closely follows the diagonal in the CDF comparison, signifying a strong alignment between the true data distribution and the distribution derived from the generative model. The result using diffeomorphic mapping is shown in Figure 6. By comparing the CDF comparison plots of two methods, the reflection based method outperforms the diffeomorphic based method, where the latter suffers from visible bias of the distribution due to the analytic blowups at edges/corners at edges/corners.

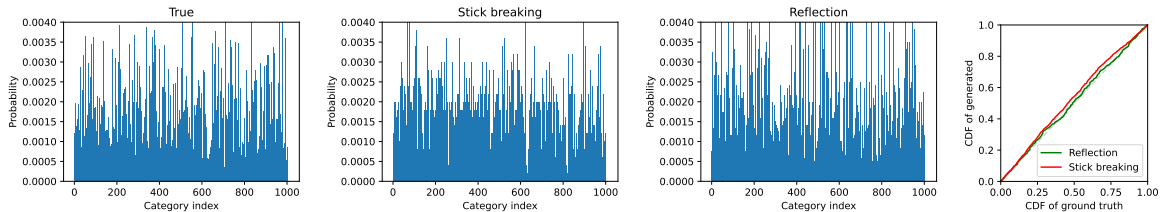


Figure 6: Generations of high-dimensional projected simplex. The results compare reflection based and stick breaking based methods.

7 Conclusion

Reflected diffusion models, which are motivated by thresholding techniques, introduce explicit score-matching loss through reflected Brownian motion. Traditionally, these models are applied to hypercube-related domains and necessitate specific diffeomorphic mappings for extension to other domains. To enhance generality with optimal transport guarantees, we introduce the Reflected Schrödinger Bridge, which employs reflected forward-backward stochastic differential equations with Neumann and Robin boundary conditions. We establish connections between dynamic and static IPF algorithms in both primal and dual formulations. Additionally, we provide an approximate linear convergence analysis of the dual, potential, and couplings to deepen our understanding of the dynamic IPF algorithm. Empirically, our algorithm can be applied to any smooth domains using RVE-SDE and RVP-SDE. We evaluate its performance on 2D synthetic examples and standard image benchmarks, underscoring its competitiveness in constrained generative modeling. In future research, our focus includes integrating nonlinear diffusion based on importance sampling [Deng et al., 2022a,b] to further expedite the generation process.

References

- Mohammadreza Armandpour, Ali Sadeghian, Chunyuan Li, and Mingyuan Zhou. Partition-guided GANs. In *Conference on Computer Vision and Pattern Recognition*, 2021.
- Nicolas Brosse, Alain Durmus, Éric Moulines, and Marcelo Pereyra. Sampling from a Log-concave Distribution with Compact Support with Proximal Langevin Monte Carlo. In *COLT*, 2017.
- Sébastien Bubeck, Ronen Eldan, and Joseph Lehec. Sampling from a Log-Concave Distribution with Projected Langevin Monte Carlo. *Discrete Comput Geom*, page 757–783, 2018.
- Charlotte Bunne, Ya-Ping Hsieh, Marco Cuturi, and Andreas Krause. The Schrödinger Bridge between Gaussian Measures has a Closed Form. In *AISTATS*, 2023.
- Kenneth F. Caluya and Abhishek Halder. Reflected Schrödinger Bridge: Density Control with Path Constraints. In *American Control Conference (ACC)*, 2021.
- Kenneth F. Caluya and Abhishek Halder. Wasserstein Proximal Algorithms for the Schrödinger Bridge Problem: Density Control with Nonlinear Drift. *IEEE Transactions on Automatic Control*, 67(3):1163–1178, 2022.
- Guillaume Carlier. On the Linear Convergence of the Multi-Marginal Sinkhorn Algorithm. *SIAM Journal on Optimization*, 32:2:10.1137, 2022.
- Patrick Cattiaux. Time Reversal of Diffusion Processes with a Boundary Condition. *Stochastic Processes and their Applications*, 28:275–292, 1988.
- Sitan Chen, Sinho Chewi, Jerry Li, Yuanzhi Li, Adil Salim, and Anru R. Zhang. Sampling is as Easy as Learning the Score: Theory for Diffusion Models with Minimal Data Assumptions. *arXiv preprint arXiv:2209.11215v2*, 2022a.
- Tianrong Chen, Guan-Hong Liu, and Evangelos A. Theodorou. Likelihood Training of Schrödinger Bridge using Forward-Backward SDEs Theory. In *Proc. of the International Conference on Learning Representation (ICLR)*, 2022b.
- Y. Chen, W. Deng, S. Fang, F. Li, N. Yang, Y. Zhang, K. Rasul, S. Zhe, A. Schneider, and Y. Nevmyvaka. Provably Convergent Schrödinger Bridge with Applications to Probabilistic Time Series Imputation. In *Proc. of the International Conference on Machine Learning (ICML)*, 2023.
- Yongxin Chen and Tryphon Georgiou. Stochastic Bridges of Linear Systems. *IEEE Transactions on Automatic Control*, 61(2), 2016.
- Yongxin Chen, Tryphon T. Georgiou, and Michele Pavon. Entropic and Displacement Interpolation: a Computational Approach using the Hilbert Metric. *SIAM Journal on Applied Mathematics*, 2016.
- Yongxin Chen, Tryphon T. Georgiou, and Michele Pavon. Stochastic Control Liaisons: Richard Sinkhorn Meets Gaspard Monge on a Schrödinger Bridge. *SIAM Review*, 63(2):249–313, 2021.
- Valentin De Bortoli. Convergence of Denoising Diffusion Models under the Manifold Hypothesis. *Transactions on Machine Learning Research (TMLR)*, 2022.
- Valentin De Bortoli, James Thornton, Jeremy Heng, and Arnaud Doucet. Diffusion Schrödinger Bridge with Applications to Score-Based Generative Modeling. In *Advances in Neural Information Processing Systems (NeurIPS)*, 2021.
- Valentin De Bortoli, Émile Mathieu, Michael Hutchinson, James Thornton, Yee Whye Teh, and Arnaud Doucet. Riemannian Score-Based Generative Modelling. In *Advances in Neural Information Processing Systems (NeurIPS)*, 2022.
- G. Deligiannidis, V. De Bortoli, and A. Doucet. Quantitative Uniform Stability of the Iterative Proportional Fitting Procedure. *Preprint arXiv:2108.08129v2*, 2021.
- Wei Deng, Siqi Liang, Botao Hao, Guang Lin, and Faming Liang. Interacting contour stochastic gradient langevin dynamics. In *Proc. of the International Conference on Learning Representation (ICLR)*, 2022a.
- Wei Deng, Guang Lin, and Faming Liang. An Adaptively Weighted Stochastic Gradient MCMC Algorithm for Monte Carlo Simulation and Global Optimization. *Statistics and Computing*, pages 32–58, 2022b.
- Prafulla Dhariwal and Alex Nichol. Diffusion Models Beat GANs on Image Synthesis. In *Advances in Neural Information Processing Systems (NeurIPS)*, 2022.
- Stephan Eckstein and Marcel Nutz. Convergence Rates for Regularized Optimal Transport via Quantization. *arXiv:2208.14391*, 2022.
- Nic Fishman, Leo Klarner, Valentin De Bortoli, Emile Mathieu, and Michael Hutchinson. Diffusion Models for Constrained Domains. *Transactions on Machine Learning Research*, 2023.

- Jiequn Han, Arnulf Jentzen, and Weinan E. Solving High-dimensional Partial Differential Equations using Deep Learning. *PNAS*, 2019.
- Jeremy Heng, Valentin De Bortoli, Arnaud Doucet, and James Thornton. Simulating Diffusion Bridges with Score Matching. In *arXiv:2111.07243*, 2022.
- Martin Heusel, Hubert Ramsauer, Thomas Unterthiner, Bernhard Nessler, and Sepp Hochreiter. Gans Trained by a Two Time-scale Update Rule Converge to a Local Nash Equilibrium. *Advances in neural information processing systems*, 30, 2017.
- Jonathan Ho, Ajay Jain, and Pieter Abbeel. Denoising Diffusion Probabilistic Models. In *Advances in Neural Information Processing Systems (NeurIPS)*, 2020.
- Jonathan Ho, William Chan, Chitwan Saharia, Jay Whang, Ruiqi Gao, Alexey Gritsenko, Diederik P. Kingma, Ben Poole, Mohammad Norouzi, David J. Fleet, and Tim Salimans. Imagen Video: High Definition Video Generation with Diffusion Models. In *arXiv:2210.02303*, 2022.
- Emiel Hoogetboom, Víctor García Satorras, Clément Vignac, and Max Welling. Equivariant Diffusion for Molecule Generation in 3D. In *Proc. of the International Conference on Machine Learning (ICML)*, 2022.
- Ya-Ping Hsieh, Ali Kavis, Paul Rolland, and Volkan Cevher. Mirrored Langevin Dynamics. In *Advances in Neural Information Processing Systems (NeurIPS)*, 2018.
- Chin-Wei Huang, Milad Aghajohari, Avishek Joey Bose, Prakash Panangaden, and Aaron Courville. Riemannian Diffusion Models. In *Advances in Neural Information Processing Systems (NeurIPS)*, 2022.
- Aapo Hyvärinen. Estimation of Non-normalized Statistical Models by Score Matching. *Journal of Machine Learning Research*, 6(24):695–709, 2005.
- Ioannis Karatzas and Steven E. Shreve. *Brownian Motion and Stochastic Calculus*. Springer, 1998.
- Frederic Koehler, Alexander Heckett, and Andrej Risteski. Statistical Efficiency of Score Matching: The View from Isoperimetry. In *ICLR*, 2023.
- Yunbum Kook, Yin Tat Lee, Ruoqi Shen, and Santosh S. Vempala. Sampling with Riemannian Hamiltonian Monte Carlo in a Constrained Space. In *NeurIPS*, 2022.
- S. Kullback. Probability Densities with Given Marginals. *Ann. Math. Statist.*, 1968.
- Andrew Lamperski. Projected Stochastic Gradient Langevin Algorithms for Constrained Sampling and Non-Convex Learning. In *Proc. of Conference on Learning Theory (COLT)*, 2021.
- Hugo Lavenant and Filippo Santambrogio. The Flow Map of the Fokker–Planck Equation Does Not Provide Optimal Transport. *Applied Mathematics Letters*, 133, 2022.
- Christian Léonard. Minimization of Energy Functionals Applied to Some Inverse Problems. *Applied Mathematics and Optimization volume*, 44:273–297, 2001.
- Christian Léonard. A Survey of the Schrödinger Problem and Some of its Connections with Optimal Transport. *Discrete & Continuous Dynamical Systems-A*, 34(4):1533–1574, 2014.
- Shuang Li, Yilun Du, Joshua B Tenenbaum, Antonio Torralba, and Igor Mordatch. Composing Ensembles of Pre-trained Models via Iterative Consensus. *ICLR*, 2023.
- P. L. Lions and A. S. Sznitman. Stochastic Differential Equations with Reflecting Boundary Conditions. *Communications on Pure and Applied Mathematics*, pages 511–537, 1984.
- Guan-Hong Liu, Tianrong Chen, Evangelos A. Theodorou, and Molei Tao. Mirror Diffusion Models for Constrained and Watermarked Generation. In *Advances in Neural Information Processing Systems (NeurIPS)*, 2023a.
- Xingchao Liu, Lemeng Wu, Mao Ye, and Qiang Liu. Learning Diffusion Bridges on Constrained Domains. In *Proc. of the International Conference on Learning Representation (ICLR)*, 2023b.
- Aaron Lou and Stefano Ermon. Reflected Diffusion Models. In *Proc. of the International Conference on Machine Learning (ICML)*, 2023.
- Cheng Lu, Yuhao Zhou, Fan Bao, Jianfei Chen, Chongxuan Li, and Jun Zhu. DPM-Solver: A Fast ODE Solver for Diffusion Probabilistic Model Sampling in Around 10 Steps. In *Advances in Neural Information Processing Systems (NeurIPS)*, 2022.
- Jin Ma and Jiongmin Yong. *Forward-Backward Stochastic Differential Equations and their Applications*. Springer, 2007.
- S. Di Marino and A. Gerolin. An Optimal Transport Approach for the Schrödinger Bridge Problem and Convergence of Sinkhorn Algorithm. *Journal of Scientific Computing*, 85:2:27–28, 2020.

- Marcel Nutz. Introduction to Entropic Optimal Transport. *Lecture Notes*, 2022.
- Marcel Nutz and Johannes Wiesel. Stability of Schrödinger Potentials and Convergence of Sinkhorn’s Algorithm. *Annals of Probability*, 2022.
- B. Øksendal. *Stochastic Differential Equations: An Introduction with Applications*. Springer, 2003.
- Seung Park and Yong-Goo Shin. Generative Residual Block for Image Generation. *Applied Intelligence*, pages 1–10, 2022.
- Grigorios A. Pavliotis. *Stochastic Processes and Applications: Diffusion Processes, the Fokker-Planck and Langevin Equations*. Springer, 2014.
- Michele Pavon, Esteban G. Tabak, and Giulio Trigila. The Data-driven Schrödinger Bridge. *Communications on Pure and Applied Mathematics*, 74:1545–1573, 2021.
- Stefano Peluchetti. Diffusion Bridge Mixture Transports, Schrödinger Bridge Problems and Generative Modeling. *ArXiv e-prints arXiv:2304.00917v1*, 2023.
- Gabriel Peyré and Marco Cuturi. *Computational Optimal Transport: With Applications to Data Science*. Foundations and Trends in Machine Learning, 2019.
- L. Ruschendorf. Convergence of the Iterative Proportional Fitting Procedure. *Ann. of Statistics*, 1995.
- Tim Salimans and Jonathan Ho. Progressive Distillation for Fast Sampling of Diffusion Models. In *Proc. of the International Conference on Learning Representation (ICLR)*, 2022.
- Yuyang Shi, Valentin De Bortoli, Andrew Campbell, and Arnaud Doucet. Diffusion Schrödinger Bridge Matching. In *arXiv:2303.16852v1*, 2023.
- A. V. Skorokhod. Stochastic Equations for Diffusion Processes in a Bounded Region. *Theory of Probability & Its Applications*, page 264–274, 1961.
- Yang Song, C. Durkan, I. Murray, and Stefano Ermon. Maximum Likelihood Training of Score-Based Diffusion Models . In *Advances in Neural Information Processing Systems (NeurIPS)*, 2021a.
- Yang Song, Jascha Sohl-Dickstein, Diederik P. Kingma, Abhishek Kumar, Stefano Ermon, and Ben Poole. Score-Based Generative Modeling through Stochastic Differential Equations . In *Proc. of the International Conference on Learning Representation (ICLR)*, 2021b.
- James Thornton, Michael Hutchinson, Emile Mathieu, Valentin De Bortoli, Yee Whye Teh, and Arnaud Doucet. Riemannian Diffusion Schrödinger Bridge. *arXiv:2207.03024v1*, 2022.
- Arash Vahdat, Karsten Kreis, and Jan Kautz. Score-based Generative Modeling in Latent Space. *Advances in Neural Information Processing Systems*, 34:11287–11302, 2021.
- Francisco Vargas, Pierre Thodoroff, Austen Lamacraft, and Neil Lawrence. Solving Schrödinger Bridges via Maximum Likelihood. *Entropy*, 23(9):1134, 2021.
- Cédric Villani. *Topics in Optimal Transportation*, volume 58. American Mathematical Soc., 2003.
- Maxime Vono, Daniel Paulin, and Arnaud Doucet. Efficient MCMC Sampling with Dimension-Free Convergence Rate using ADMM-type Splitting. *Journal of Machine Learning Research*, 2022.
- R. J. Williams. *On Time-Reversal of Reflected Brownian Motions*. Part of the Progress in Probability and Statistics book series, 1987.

Notations Ω is the bounded domain of interest, $\partial\Omega$ denotes the boundary, and D is the radius of a ball centered at the origin that covers Ω . $\nabla \cdot$ and ∇ denote the divergence and gradient operator (with respect to \mathbf{x}). ε is the entropic regularizer; ϵ controls the perturbation of the marginals. c_ε and c are cost functions in EOT, and $c_\varepsilon = c/\varepsilon$. ψ_\star and φ_\star are the Schrödinger potentials; $\nabla \log \overrightarrow{\psi}(\mathbf{x}_t, t)$ and $\nabla \log \overleftarrow{\varphi}(\mathbf{x}_t, t)$ are the forward-backward score functions in reflected FB-SDE. $\mathcal{D}(\mu_\star, \nu_\star) \subset C(\Omega, [0, T])$ is the path space with marginals μ_\star (data distribution) at time $t = 0$ and ν_\star (prior distribution) at $t = T$, $\Pi(\mu_\star, \nu_\star) \subset \Omega^2$ is the product space containing couplings with the first marginal μ_\star and second marginal ν_\star .

8 Reflected Forward-Backward SDE

8.1 From Reflected Schrödinger Bridge to Reflected FB-SDE

We consider the stochastic control of the reflected SBP

$$\begin{aligned} & \inf_{\mathbf{u} \in \mathcal{U}} \mathbb{E} \left\{ \int_0^T \frac{1}{2} \|\mathbf{u}(\mathbf{x}, t)\|_2^2 dt \right\} \\ \text{s.t. } & d\mathbf{x}_t = [\mathbf{f}(\mathbf{x}, t) + g(t)\mathbf{u}(\mathbf{x}, t)] dt + \sqrt{2\varepsilon}g(t)d\mathbf{w}_t + \mathbf{n}(\mathbf{x})d\mathbf{L}_t \\ & \mathbf{x}_0 \sim \mu_\star, \quad \mathbf{x}_T \sim \nu_\star, \quad \mathbf{x}_t \in \Omega, \end{aligned} \quad (17)$$

where Ω is the state-space of \mathbf{x} and $\mathbf{u} : \Omega \times [0, T] \rightarrow \mathbb{R}^d$ is the control variable in the space of \mathcal{U} ; $\mathbf{f} : \Omega \times [0, T] \rightarrow \mathbb{R}^d$ is the vector field; \mathbf{w}_t denotes the Brownian motion; The expectation is evaluated w.r.t the PDF $\rho(\mathbf{x}, t)$ of (17); ε is the diffusion term and also the entropic regularizer; \mathbf{L} is the local time supported on $\{t \in [0, T] | \mathbf{x}_t \in \partial\Omega\}$ and forces the particle to go back to Ω . More precisely, \mathbf{L} is a continuous non-decreasing process with $\mathbf{L}_0 = 0$ and it increases only when \mathbf{x}_t hits the boundary $\partial\Omega$, that is,

$$\mathbf{L}_t = \int_0^t \mathbf{1}_{\{\mathbf{x}_s \in \partial\Omega\}} d\mathbf{L}_s. \quad (18)$$

The existence and uniqueness of SDE (17) can be addressed through the so-called *Skorokhod problem* [Skorokhod, 1961] which amounts to finding the decomposition for any given continuous path $\mathbf{w}_t \in C(\mathbb{R}^d, [0, T])$, there exists a pair $(\mathbf{y}_t, \mathbf{L}_t)$ such that

$$\mathbf{w}_t = \mathbf{y}_t + \mathbf{L}_t,$$

where $\mathbf{y}_t \in C(\Omega, [0, T])$ and \mathbf{L}_t satisfies (18) [Lions and Sznitman, 1984].

Rewrite reflected SBP into a variational form [Chen et al., 2021]

$$\inf_{\mathbf{u} \in \mathcal{U}, \rho} \int_0^T \int_{\Omega} \frac{1}{2} \|\mathbf{u}(\mathbf{x}, t)\|_2^2 \rho(\mathbf{x}, t) d\mathbf{x} dt \quad (19)$$

$$\text{s.t. } \frac{\partial \rho}{\partial t} + \nabla \cdot \mathbf{J}|_{\mathbf{x} \in \Omega} = 0, \quad \langle \mathbf{J}, \mathbf{n} \rangle|_{\mathbf{x} \in \partial\Omega} = 0, \quad (20)$$

where \mathbf{J} is the probability flux of continuity equation [Pavliotis, 2014] given by

$$\mathbf{J} \equiv \rho(\mathbf{f} + g\mathbf{u}) - \varepsilon g^2 \nabla \rho. \quad (21)$$

Explore the Lagrangian of (19) and incorporate a multiplier: $\phi(\mathbf{x}, t) : \Omega \times [0, T] \rightarrow \mathbb{R}$

$$\begin{aligned} \mathcal{L}(\rho, \mathbf{u}, \phi) &= \int_0^T \int_{\Omega} \frac{1}{2} \|\mathbf{u}\|_2^2 \rho + \phi \left(\frac{\partial \rho}{\partial t} + \nabla \cdot \mathbf{J} \right) d\mathbf{x} dt \\ &= \int_0^T \int_{\Omega} \left(\frac{1}{2} \rho \|\mathbf{u}\|_2^2 - \rho \frac{\partial \phi}{\partial t} - \langle \nabla \phi, \mathbf{J} \rangle \right) d\mathbf{x} dt + \underbrace{\int_{\Omega} \phi \rho|_{t=0}^T d\mathbf{x}}_{\text{constant term}} + \underbrace{\int_0^T \int_{\partial\Omega} \langle \mathbf{J}, \mathbf{n} \rangle d\sigma(\mathbf{x}) dt}_{:=0 \text{ by Eq.(20)}} \end{aligned} \quad (22)$$

where the second equation follows by Stokes' theorem.

Plugging (21) into (22) and ignoring constant terms, we have

$$\bar{\mathcal{L}}(\rho, \mathbf{u}, \phi) = \int_0^T \int_{\Omega} \left(\frac{1}{2} \rho \|\mathbf{u}\|_2^2 - \rho \frac{\partial \phi}{\partial t} - \langle \nabla \phi, \rho(\mathbf{f} + g\mathbf{u}) - \varepsilon g^2 \nabla \rho \rangle \right) d\mathbf{x} dt. \quad (23)$$

The optimal control \mathbf{u}^* follows by taking gradient with respect to \mathbf{u}

$$\mathbf{u}^*(\mathbf{x}, t) = g(t)\nabla\phi(\mathbf{x}, t). \quad (24)$$

Plugging $\mathbf{u}^*(\mathbf{x}, t)$ into (23) and setting $\bar{\mathcal{L}}(\rho, \mathbf{u}^*, \phi) \equiv 0$, we apply integration by parts and derive

$$\begin{aligned} 0 &= - \int_0^T \int_{\Omega} \left(\frac{1}{2} \rho g^2 \|\nabla\phi\|_2^2 + \rho \frac{\partial\phi}{\partial t} + \rho \langle \nabla\phi, \mathbf{f} \rangle - \varepsilon g^2 \langle \nabla\phi, \nabla\rho \rangle \right) d\mathbf{x}dt \\ &= - \int_0^T \int_{\Omega} \rho \left(\frac{1}{2} g^2 \|\nabla\phi\|_2^2 + \frac{\partial\phi}{\partial t} + \langle \nabla\phi, \mathbf{f} \rangle + \varepsilon g^2 \Delta\phi \right) d\mathbf{x}dt + \int_0^T \int_{\partial\Omega} \varepsilon g^2 \rho \langle \nabla\phi, \mathbf{n} \rangle d\sigma(\mathbf{x})dt. \end{aligned}$$

This yields the following constrained *Hamilton–Jacobi–Bellman* (HJB) PDE:

$$\begin{cases} \frac{\partial\phi}{\partial t} + \varepsilon g^2 \Delta\phi + \langle \nabla\phi, \mathbf{f} \rangle = -\frac{1}{2} \|g(t)\nabla\phi(\mathbf{x}, t)\|_2^2 & \text{in } \Omega \\ \langle \nabla\phi, \mathbf{n} \rangle = 0 & \text{on } \partial\Omega. \end{cases}$$

Applying the Cole-Hopf transformation:

$$\vec{\psi}(\mathbf{x}, t) = \exp\left(\frac{\phi(\mathbf{x}, t)}{2\varepsilon}\right), \quad \phi(\mathbf{x}, t) = 2\varepsilon \log \vec{\psi}(\mathbf{x}, t), \quad (25)$$

then we see that $\vec{\psi}$ satisfies a backward Kolmogorov equation with Neumann boundary condition

$$\begin{cases} \frac{\partial\vec{\psi}}{\partial t} + \varepsilon g^2 \Delta\vec{\psi} + \langle \nabla\vec{\psi}, \mathbf{f} \rangle = 0 & \text{in } \Omega \\ \langle \nabla\vec{\psi}, \mathbf{n} \rangle = 0 & \text{on } \partial\Omega. \end{cases}$$

On the other hand, we set

$$\overleftarrow{\varphi}(\mathbf{x}, t) = \rho^*(\mathbf{x}, t) / \vec{\psi}(\mathbf{x}, t), \quad (26)$$

where $\rho^*(\mathbf{x}, t)$ is the probability density of Eq.(19) given the optimal control variable \mathbf{u}^* . Then from $\rho^* = \overleftarrow{\varphi} \vec{\psi}$, Eq.(20) can be further simplified to

$$\begin{aligned} 0 &= \partial_t \rho^* + \nabla \cdot \left[\rho^* (\mathbf{f} + g\mathbf{u}^*) - \varepsilon g^2 \nabla \rho^* \right] \\ &= \partial_t (\overleftarrow{\varphi} \vec{\psi}) + \nabla \cdot \left[\overleftarrow{\varphi} \vec{\psi} (\mathbf{f} + g^2 \nabla \phi) - \varepsilon g^2 \nabla (\overleftarrow{\varphi} \vec{\psi}) \right] \\ &= (\partial_t \overleftarrow{\varphi}) \vec{\psi} + \overleftarrow{\varphi} (\partial_t \vec{\psi}) + \nabla \cdot \left[\overleftarrow{\varphi} \vec{\psi} (\mathbf{f} + 2\varepsilon g^2 \nabla \log \vec{\psi}) \right] - \varepsilon g^2 \Delta (\overleftarrow{\varphi} \vec{\psi}) \\ &= \dots = \vec{\psi} \left(\partial_t \overleftarrow{\varphi} + \nabla \cdot (\overleftarrow{\varphi} \mathbf{f} - \varepsilon g^2 \nabla \overleftarrow{\varphi}) \right), \end{aligned}$$

where we use the identity $\Delta(\vec{\psi} \overleftarrow{\varphi}) = \overleftarrow{\varphi} \Delta \vec{\psi} + \Delta \overleftarrow{\varphi} \vec{\psi} + 2\langle \nabla \vec{\psi}, \nabla \overleftarrow{\varphi} \rangle$. Then we arrive at the forward Kolmogorov equation with the Robin boundary condition

$$\begin{cases} \partial_t \overleftarrow{\varphi} + \nabla \cdot (\overleftarrow{\varphi} \mathbf{f} - \varepsilon g^2 \nabla \overleftarrow{\varphi}) = 0 & \text{in } \Omega \\ \langle \overleftarrow{\varphi} \mathbf{f} - \varepsilon g^2 \nabla \overleftarrow{\varphi}, \mathbf{n} \rangle = 0 & \text{on } \partial\Omega, \end{cases}$$

where the second boundary condition follows by invoking the Stokes' theorem for the first equation.

Plugging Eq.(24) and Eq.(25) into Eq.(17), the backward PDE corresponds to the forward SDE

$$d\mathbf{x}_t = \left[\mathbf{f}(\mathbf{x}_t, t) + 2\varepsilon g(t)^2 \nabla \log \vec{\psi}(\mathbf{x}_t, t) \right] dt + \sqrt{2\varepsilon} g(t) d\mathbf{w}_t + \mathbf{n}(\mathbf{x}) d\mathbf{L}_t, \quad \mathbf{x}_0 \sim \mu_*$$

Reversing the forward SDE [Williams, 1987, Cattiaux, 1988] with $\log \vec{\psi}(\cdot, t) + \log \overleftarrow{\varphi}(\cdot, t) = \log \rho^*(\cdot, t)$ based on Eq.(26), we arrive at the backward SDE

$$d\mathbf{x}_t = \left[\mathbf{f}(\mathbf{x}_t, t) - 2\varepsilon g(t)^2 \nabla \log \overleftarrow{\varphi}(\mathbf{x}_t, t) \right] dt + \sqrt{2\varepsilon} g(t) d\bar{\mathbf{w}}_t + \mathbf{n}(\mathbf{x}) d\bar{\mathbf{L}}_t, \quad \mathbf{x}_T \sim \nu_*$$

Our derivation is in a spirit similar to Caluya and Halder [2021]. The difference is that the proof is derived from the perspective of probability flux and enables us to derive the Neunman and Robin boundaries more explicitly.

Remark 1. Regarding the scores $\nabla \log \vec{\psi}$ and $\nabla \log \overleftarrow{\varphi}$ at $t = 0$ and T , we follow the standard truncation techniques [Ho et al., 2020, Fishman et al., 2023] and fix them to $\mathbf{0}$. We refer readers to Appendix C of Song et al. [2021b] and Appendix B of Song et al. [2021a] for more discussions.

8.2 Connections between reflected FB-SDEs and flow-based models

Similar to Fishman et al. [2023], Lou and Ermon [2023], our flow representation in Eq.(20) together with (26) naturally yields

Proposition 3 (Probability Flow ODE). *Consider the reflected FB-SDEs (6) with Neumann and Robin boundary conditions. The corresponding probability flow ODE is given by*

$$d\mathbf{x}_t = \left[\mathbf{f}(\mathbf{x}_t, t) + \varepsilon g(t)^2 (\nabla \log \vec{\psi}(\mathbf{x}_t, t) - \nabla \log \overleftarrow{\varphi}(\mathbf{x}_t, t)) \right] dt.$$

The result is the same as in Chen et al. [2022b] and provides a stable alternative to compute the log-likelihood of the data.

9 Convergence of dual, potentials, and couplings

Next, we modify Algorithm 2 following the centering method developed in [Carlier, 2022].

Algorithm 3 Centered Sinkhorn. Set $\bar{\varphi}_0 := 0$. For $k \geq 0$, the iterate follows

$$\bar{\psi}_k(\mathbf{y}) := -\log \int_{\Omega} e^{\bar{\varphi}_k(\mathbf{x}) - c_\varepsilon(\mathbf{x}, \mathbf{y})} \mu_{\star, k}(\mathbf{d}\mathbf{x}) \quad (27)$$

$$\bar{\varphi}_{k+1}(\mathbf{x}) := -\log \int_{\Omega} e^{\bar{\psi}_k(\mathbf{y}) - c_\varepsilon(\mathbf{x}, \mathbf{y})} \nu_{\star, k}(\mathbf{d}\mathbf{y}) + \lambda_k, \quad \text{where} \quad (28)$$

$$\lambda_k := \int_{\Omega} \log \left(\int_{\Omega} e^{\bar{\psi}_k(\mathbf{y}) - c_\varepsilon(\mathbf{x}, \mathbf{y})} \nu_{\star, k}(\mathbf{d}\mathbf{y}) \right) \mu_{\star}(\mathbf{d}\mathbf{x}).$$

The algorithm differs from Algorithm 2 in that an additional centering operation is included in the updates of $\bar{\varphi}_{k+1}$ to ensure $\mu_{\star}(\bar{\varphi}_{k+1}) = 0$. Notably, μ_{\star} is required for the centering operation to upper bound the divergence, although it is not directly accessible and no implementation is needed. The main contribution of the centering operation is that the two coordinates $(\bar{\varphi}, \bar{\psi})$ become separable

$$\|\bar{\varphi} \oplus \bar{\psi}\|_{L^2(\mu_{\star} \otimes \nu_{\star})}^2 = \|\bar{\varphi}\|_{L^2(\mu_{\star})}^2 + \|\bar{\psi}\|_{L^2(\nu_{\star})}^2 \quad \text{if } \mu_{\star}(\bar{\varphi}) = 0. \quad (29)$$

The coordinate ascent is equivalent to the following updates

$$\bar{\psi}_k(y) = \arg \max_{\bar{\psi} \in L^1(\nu_{\star})} G(\bar{\varphi}_k, \bar{\psi}), \quad \bar{\varphi}_k(y) = \arg \max_{\bar{\varphi} \in L^1(\mu_{\star}) : \mu_{\star}(\bar{\varphi})=0} G(\bar{\varphi}, \bar{\psi}_k).$$

The relation between the Schrödinger potentials (φ_k, ψ_k) and centered Schrödinger potentials $(\bar{\varphi}_k, \bar{\psi}_k)$ is characterized as follows

Lemma 3. *Denote by (φ_k, ψ_k) the Sinkhorn iterates in Algorithm 2. For all $k \geq 0$, $\mu_{\star}(\varphi_k) = -(\lambda_0 + \dots + \lambda_{k-1})$. Moreover, we have*

$$\bar{\varphi}_k = \varphi_k - \mu_{\star}(\varphi_k), \quad \bar{\psi}_k = \psi_k + \mu_{\star}(\psi_k).$$

In particular, $\bar{\varphi}_k \oplus \bar{\psi}_k = \varphi_k \oplus \psi_k$ and $G(\bar{\varphi}_k, \bar{\psi}_k) = G(\varphi_k, \psi_k)$.

Proof Applying the induction method completes the proof directly. □

Recall how $\bar{\psi}_k$ is defined through the Schrödinger equation

$$\text{The second marginal of } \pi_{2k}(\bar{\varphi}_k, \bar{\psi}_k) = e^{\bar{\varphi}_k \oplus \bar{\psi}_k - c_\varepsilon} d(\mu_{\star, k} \otimes \nu_{\star, k}) \text{ is } \nu_{\star, k},$$

as in Eq.(14). However, $d\pi_{2k+1}(\bar{\varphi}_{k+1}, \bar{\psi}_k) = e^{\bar{\varphi}_{k+1} \oplus \bar{\psi}_k - c_\varepsilon} d(\mu_{\star, k} \otimes \nu_{\star, k})$ fails to yield the first marginal $\mu_{\star, k}$ due to the centering constraint.

Next, we show the modified iterates are bounded by the cost function c .

Lemma 4. *For every $k \geq 0$, the potentials are bounded by*

$$\|\bar{\varphi}_k\|_{\infty} \leq 2\|c_\varepsilon\|_{\infty}, \quad \|\bar{\psi}_k\|_{\infty} \leq 3\|c_\varepsilon\|_{\infty}.$$

Proof By Assumption A1, the transition kernel $\mathcal{K}(\mathbf{x}, \mathbf{y}) = e^{-c_\varepsilon(\mathbf{x}, \mathbf{y})}$ associated with $\mathbf{x}_t = \mathbf{f}(\mathbf{x}_t, t)dt + \sqrt{2\varepsilon}g(t)d\mathbf{w}_t + \mathbf{n}(\mathbf{x})d\mathbf{L}_t$ is smooth in Ω , hence the cost function is Lipschitz continuous, which implies the cost function is bounded (denoted by a constant c_ε).

Recall the definition of $\bar{\varphi}_{k+1}$ in Algorithm 3, we have $\forall \mathbf{x}_1, \mathbf{x}_2 \in \Omega$,

$$\begin{aligned} & \bar{\varphi}_{k+1}(\mathbf{x}_1) - \bar{\varphi}_{k+1}(\mathbf{x}_2) \\ &= \log \int_{\Omega} e^{\bar{\psi}_k(\mathbf{y}) - c_\varepsilon(\mathbf{x}_2, \mathbf{y})} \nu_{*,k}(\mathbf{d}\mathbf{y}) - \log \int_{\Omega} e^{\bar{\psi}_k(\mathbf{y}) - c_\varepsilon(\mathbf{x}_1, \mathbf{y})} \nu_{*,k}(\mathbf{d}\mathbf{y}) \\ &\leq \log \left[e^{\sup_{\mathbf{y} \in \Omega} |c_\varepsilon(\mathbf{x}_1, \mathbf{y}) - c_\varepsilon(\mathbf{x}_2, \mathbf{y})|} \int_{\Omega} e^{\bar{\psi}_k(\mathbf{y}) - c_\varepsilon(\mathbf{x}_1, \mathbf{y})} \nu_{*,k}(\mathbf{d}\mathbf{y}) \right] - \log \int_{\Omega} e^{\bar{\psi}_k(\mathbf{y}) - c_\varepsilon(\mathbf{x}_1, \mathbf{y})} \nu_{*,k}(\mathbf{d}\mathbf{y}) \\ &= \sup_{\mathbf{y} \in \Omega} |c_\varepsilon(\mathbf{x}_1, \mathbf{y}) - c_\varepsilon(\mathbf{x}_2, \mathbf{y})| \leq 2\|c_\varepsilon\|_\infty. \end{aligned}$$

As $\mu_*(\bar{\varphi}_k) = 0$, we have $\sup_x \bar{\varphi}_k(\mathbf{x}) \geq 0$ and $\inf_x \bar{\varphi}_k(\mathbf{x}) \leq 0$, hence the above implies $\|\bar{\varphi}_k\|_\infty \leq 2\|c_\varepsilon\|_\infty$. The definition of $\bar{\psi}_k$ in Eq.(27) yields $\|\bar{\psi}_k\|_\infty \leq \|\bar{\varphi}_k\|_\infty + \|c_\varepsilon\|_\infty \leq 3\|c_\varepsilon\|_\infty$. \square

The key to the proof is to adopt the strong convexity of the function e^x for $x \in [-\alpha, \infty)$ and some constant $\alpha \in \mathbb{R}$,

$$e^b - e^a \geq (b - a)e^a + \frac{e^{-\alpha}}{2}|b - a|^2 \quad \text{for } a, b \in [-\alpha, \infty). \quad (30)$$

We also present two supporting lemmas in order to complete the proof

Lemma 5. Given $\varphi, \varphi' \in L^2(\mu_*)$ and $\psi, \psi' \in L^2(\nu_*)$, and define

$$\begin{aligned} \partial_1 G(\varphi, \psi)(\mathbf{x}) &= 1 - \int_{\Omega} e^{\varphi(\mathbf{x}) + \psi(\mathbf{y}) - c_\varepsilon(\mathbf{x}, \mathbf{y})} \nu_*(\mathbf{d}\mathbf{y}) \\ \partial_2 G(\varphi, \psi)(\mathbf{y}) &= 1 - \int_{\Omega} e^{\varphi(\mathbf{x}) + \psi(\mathbf{y}) - c_\varepsilon(\mathbf{x}, \mathbf{y})} \mu_*(\mathbf{d}\mathbf{x}). \end{aligned} \quad (31)$$

If both $\varphi \otimes \psi - c_\varepsilon \geq -\alpha$ and $\varphi' \oplus \psi' - c_\varepsilon \geq -\alpha$ for some $\alpha \in \mathbb{R}$, we have

$$\begin{aligned} G(\varphi', \psi') - G(\varphi, \psi) &\geq \int_{\Omega} \partial_1 G(\varphi', \psi')(\mathbf{x})[\varphi'(\mathbf{x}) - \varphi(\mathbf{x})] \mu_*(\mathbf{d}\mathbf{x}) \\ &\quad + \int_{\Omega} \partial_2 G(\varphi', \psi')(\mathbf{y})[\psi'(\mathbf{y}) - \psi(\mathbf{y})] \nu_*(\mathbf{d}\mathbf{y}) \\ &\quad + \frac{e^{-\alpha}}{2} \|(\varphi - \varphi') \oplus (\psi - \psi')\|_{L^2(\mu_* \otimes \nu_*)}. \end{aligned}$$

Proof By Eq.(30), we have

$$\begin{aligned} & G(\varphi', \psi') - G(\varphi, \psi) \\ &= \mu_*(\varphi' - \varphi) + \nu_*(\psi' - \psi) + \iint_{\Omega^2} (e^{\varphi \oplus \psi - c_\varepsilon} - e^{\varphi' \oplus \psi' - c_\varepsilon}) d(\mu_* \otimes \nu_*) \\ &\geq \mu_*(\varphi' - \varphi) + \nu_*(\psi' - \psi) + \iint_{\Omega^2} (\varphi \oplus \psi - \varphi' \oplus \psi') e^{\varphi' \oplus \psi' - c_\varepsilon} d(\mu_* \otimes \nu_*) \\ &\quad + \frac{e^{-\alpha}}{2} \iint_{\Omega^2} \|\varphi \oplus \psi - \varphi' \oplus \psi'\|_2^2 d(\mu_* \otimes \nu_*) \\ &= \int_{\Omega} \partial_1 G(\varphi', \psi')(\mathbf{x})[\varphi'(\mathbf{x}) - \varphi(\mathbf{x})] \mu_*(\mathbf{d}\mathbf{x}) + \int_{\Omega} \partial_2 G(\varphi', \psi')(\mathbf{y})[\psi'(\mathbf{y}) - \psi(\mathbf{y})] \nu_*(\mathbf{d}\mathbf{y}) \\ &\quad + \frac{e^{-\alpha}}{2} \|(\varphi - \varphi') \oplus (\psi - \psi')\|_{L^2(\mu_* \otimes \nu_*)}. \end{aligned}$$

\square

Lemma 6. Given a small $\epsilon \leq \frac{1}{(D+1)^2}$, we have

$$G(\bar{\varphi}_{k+1}, \bar{\psi}_{k+1}) - G(\bar{\varphi}_k, \bar{\psi}_k) \geq \frac{\sigma}{2} \left(\|\bar{\varphi}_{k+1} - \bar{\varphi}_k\|_{L^2(\mu_*)}^2 + \|\bar{\psi}_{k+1} - \bar{\psi}_k\|_{L^2(\nu_*)}^2 \right) - O(\epsilon),$$

where $\sigma := e^{-6\|c_\varepsilon\|_\infty}$; the big-O notation mainly depends on volume of the domain Ω .

Proof We first decompose the LHS as follows

$$G(\bar{\varphi}_{k+1}, \bar{\psi}_{k+1}) - G(\bar{\varphi}_k, \bar{\psi}_k) = \underbrace{G(\bar{\varphi}_{k+1}, \bar{\psi}_{k+1}) - G(\bar{\varphi}_{k+1}, \bar{\psi}_k)}_I + \underbrace{G(\bar{\varphi}_{k+1}, \bar{\psi}_k) - G(\bar{\varphi}_k, \bar{\psi}_k)}_{II}.$$

For the estimate of I, by Lemma 5 with $\sigma = e^{-6\|c_\varepsilon\|_\infty}$, we have

$$I \geq \int_{\Omega} \partial_2 G(\bar{\varphi}_{k+1}, \bar{\psi}_{k+1})(\mathbf{y}) [\bar{\psi}_{k+1}(\mathbf{y}) - \bar{\psi}_k(\mathbf{y})] \nu_\star(\mathbf{d}\mathbf{y}) + \frac{\sigma}{2} \|\bar{\psi}_k - \bar{\psi}_{k+1}\|_{L^2(\nu_\star)}.$$

For the integral above, by the definition of $\partial_2 G$ in Eq.(31), we have

$$\begin{aligned} & \partial_2 G(\bar{\varphi}_{k+1}, \bar{\psi}_{k+1})(\mathbf{y}) \nu_\star(\mathbf{d}\mathbf{y}) \\ &= \nu_\star(\mathbf{d}\mathbf{y}) - \int_{\Omega} e^{\bar{\varphi}_{k+1}(\mathbf{x}) + \bar{\psi}_{k+1}(\mathbf{y}) - c_\varepsilon(\mathbf{x}, \mathbf{y})} \mu_\star(\mathbf{d}\mathbf{x}) \nu_\star(\mathbf{d}\mathbf{y}) \\ &= \nu_\star(\mathbf{d}\mathbf{y}) - \int_{\Omega} \pi_{2k+2}(\mathbf{d}\mathbf{x}, \cdot) \frac{\mathbf{d}\mu_\star \otimes \mathbf{d}\nu_\star}{\mathbf{d}\mu_{\star, k+1} \otimes \mathbf{d}\nu_{\star, k+1}}, \end{aligned} \quad (32)$$

where the last equality follows by the LHS of Eq.(15), the last integral is with respect to \mathbf{x} .

Apply Lemma 7 with respect to $\frac{\mathbf{d}\mu_\star}{\mathbf{d}\mu_{\star, k+1}}(\mathbf{x})$

$$\begin{aligned} \int_{\Omega} \pi_{2k+2}(\mathbf{d}\mathbf{x}, \cdot) \frac{\mathbf{d}\mu_\star \otimes \mathbf{d}\nu_\star}{\mathbf{d}\mu_{\star, k+1} \otimes \mathbf{d}\nu_{\star, k+1}} &\leq \int_{\Omega} (1 + O(\varepsilon)) \pi_{2k+2}(\mathbf{d}\mathbf{x}, \cdot) \frac{\nu_\star(\mathbf{d}\mathbf{y})}{\nu_{\star, k+1}(\mathbf{d}\mathbf{y})} \\ &\leq (1 + O(\varepsilon)) \nu_{\star, k+1}(\mathbf{d}\mathbf{y}) \frac{\nu_\star(\mathbf{d}\mathbf{y})}{\nu_{\star, k+1}(\mathbf{d}\mathbf{y})} \\ &= (1 + O(\varepsilon)) \nu_\star(\mathbf{d}\mathbf{y}), \end{aligned} \quad (33)$$

where the second inequality is derived by the fact that the second marginal of π_{2k+2} is $\nu_{\star, k+1}$ in Eq.(14). Similarly, we can show $\int_{\Omega} \pi_{2k+2}(\mathbf{d}\mathbf{x}, \cdot) \frac{\mathbf{d}\mu_\star \otimes \mathbf{d}\nu_\star}{\mathbf{d}\mu_{\star, k+1} \otimes \mathbf{d}\nu_{\star, k+1}} \gtrsim (1 - O(\varepsilon)) \nu_\star(\mathbf{d}\mathbf{y})$.

Combining Eq.(32) and (33), we have

$$|\partial_2 G(\bar{\varphi}_{k+1}, \bar{\psi}_{k+1})(\mathbf{y}) \nu_\star(\mathbf{d}\mathbf{y})| \lesssim \varepsilon \nu_\star(\mathbf{d}\mathbf{y}). \quad (34)$$

We now build the lower bound of the integral as follows

$$\begin{aligned} & \int_{\Omega} \partial_2 G(\bar{\varphi}_{k+1}, \bar{\psi}_{k+1})(\mathbf{y}) [\bar{\psi}_{k+1}(\mathbf{y}) - \bar{\psi}_k(\mathbf{y})] \nu_\star(\mathbf{d}\mathbf{y}) \\ &\gtrsim -\varepsilon \int_{\Omega} |\bar{\psi}_{k+1}(\mathbf{y}) - \bar{\psi}_k(\mathbf{y})| \nu_\star(\mathbf{d}\mathbf{y}) \\ &\gtrsim -\varepsilon, \end{aligned} \quad (35)$$

where the first inequality follows by Eq.(32) and the second inequality follows by the boundedness of the potential function in Lemma 4. The above means that $I \geq \frac{\sigma}{2} \|\bar{\psi}_k - \bar{\psi}_{k+1}\|_{L^2(\mu_\star \otimes \nu_\star)} - O(\varepsilon)$. For the estimate of II, Lemma 5 yields

$$II \geq \int_{\Omega} \partial_1 G(\bar{\varphi}_{k+1}, \bar{\psi}_k)(\mathbf{x}) [\bar{\varphi}_{k+1}(\mathbf{x}) - \bar{\varphi}_k(\mathbf{x})] \mu_\star(\mathbf{d}\mathbf{x}) + \frac{\sigma}{2} \|\bar{\varphi}_k - \bar{\varphi}_{k+1}\|_{L^2(\mu_\star)}.$$

Recall the definition of $\bar{\varphi}_{k+1}$ in Eq.(28) states that $\int_{\Omega} e^{\bar{\psi}_k(\mathbf{y}) - c_\varepsilon(\mathbf{x}, \mathbf{y})} \nu_{\star, k}(\mathbf{d}\mathbf{y}) = e^{-\bar{\varphi}_{k+1}(\mathbf{x}) + \lambda_k}$. Apply Lemma 7 with respect to $\frac{\mathbf{d}\nu_\star}{\mathbf{d}\nu_{\star, k}}(\mathbf{y})$

$$\begin{aligned} \partial_1 G(\bar{\varphi}_{k+1}, \bar{\psi}_k)(\mathbf{x}) &= 1 - e^{\bar{\varphi}_{k+1}(\mathbf{x})} \int_{\Omega} e^{\bar{\psi}_k(\mathbf{y}) - c_\varepsilon(\mathbf{x}, \mathbf{y})} \nu_{\star, k}(\mathbf{d}\mathbf{y}) \frac{\nu_\star(\mathbf{d}\mathbf{y})}{\nu_{\star, k}(\mathbf{d}\mathbf{y})} \\ &\geq 1 - e^{\bar{\varphi}_{k+1}(\mathbf{x})} \int_{\Omega} (1 + O(\varepsilon)) e^{\bar{\psi}_k(\mathbf{y}) - c_\varepsilon(\mathbf{x}, \mathbf{y})} \nu_{\star, k}(\mathbf{d}\mathbf{y}) \\ &\geq 1 - (1 + O(\varepsilon)) e^{\lambda_k} - O(\varepsilon) \underbrace{\int_{\Omega} \|\mathbf{y}\|_2^2 e^{\bar{\varphi}_{k+1}(\mathbf{x}) + \bar{\psi}_k(\mathbf{y}) - c_\varepsilon(\mathbf{x}, \mathbf{y})} \nu_{\star, k}(\mathbf{d}\mathbf{y})}_{\text{bounded and non-negative from Lemma 4}} \\ &= 1 - (1 + O(\varepsilon)) e^{\lambda_k} - O(\varepsilon) \\ \partial_1 G(\bar{\varphi}_{k+1}, \bar{\psi}_k)(\mathbf{x}) &\leq 1 + (1 + O(\varepsilon)) e^{\lambda_k} + O(\varepsilon), \end{aligned}$$

which includes a deterministic scalar (independent of \mathbf{x}) and a small perturbation (dependent of \mathbf{x} and ϵ). Denote $R(\mathbf{x}, \mathbf{y}) = \|\mathbf{y}\|_2^2 e^{\bar{\varphi}_{k+1}(\mathbf{x}) + \bar{\psi}_k(\mathbf{y}) - c_\epsilon(\mathbf{x}, \mathbf{y})}$, Combining the centering operation with $\mu_\star(\bar{\varphi}_{k+1}) = \mu_\star(\bar{\varphi}_k) = 0$

$$\begin{aligned} & \int_{\Omega} \partial_1 G(\bar{\varphi}_{k+1}, \bar{\psi}_k)(\mathbf{x}) [\bar{\varphi}_{k+1}(\mathbf{x}) - \bar{\varphi}_k(\mathbf{x})] \mu_\star(d\mathbf{x}) \\ &= \text{deterministic scalar} \cdot \underbrace{\int_{\Omega} [\bar{\varphi}_{k+1}(\mathbf{x}) - \bar{\varphi}_k(\mathbf{x})] \mu_\star(d\mathbf{x})}_{:=0 \text{ by the centering operation}} + \epsilon \underbrace{\int_{\Omega} R(\mathbf{x}) [\bar{\varphi}_{k+1}(\mathbf{x}) - \bar{\varphi}_k(\mathbf{x})] \mu_\star(d\mathbf{x})}_{\text{integrable by the boundedness of } R, \bar{\varphi}_{k+1}, \bar{\psi}_k} \\ &= O(\epsilon). \end{aligned}$$

Combining the estimates of I and II completes the proof. \square

9.1 Convergence of Dual and Potentials

Proof of Lemma 2

Part I: Convergence of the Dual

By Lemma 5 with $\alpha = 6\|c\|_\infty$ and the decomposition in Eq.(29), we have

$$\begin{aligned} & G(\bar{\varphi}_k, \bar{\psi}_k) - G(\bar{\varphi}_\star, \bar{\psi}_\star) \\ & \geq \int_{\Omega} \partial_1 G(\bar{\varphi}_k, \bar{\psi}_k)(\mathbf{x}) [\bar{\varphi}_k(\mathbf{x}) - \bar{\varphi}_\star(\mathbf{x})] \mu_\star(d\mathbf{x}) \\ & \quad + \int_{\Omega} \partial_2 G(\bar{\varphi}_k, \bar{\psi}_k)(\mathbf{y}) [\bar{\psi}_k(\mathbf{y}) - \bar{\psi}_\star(\mathbf{y})] \nu_\star(d\mathbf{y}) \\ & \quad + \frac{\sigma}{2} \left(\|\bar{\varphi}_k - \bar{\varphi}_\star\|_{L^2(\mu_\star)}^2 + \|\bar{\psi}_k - \bar{\psi}_\star\|_{L^2(\nu_\star)}^2 \right) \\ & \geq \int_{\Omega} \partial_1 G(\bar{\varphi}_k, \bar{\psi}_k)(\mathbf{x}) [\bar{\varphi}_k(\mathbf{x}) - \bar{\varphi}_\star(\mathbf{x})] \mu_\star(d\mathbf{x}) + \frac{\sigma}{2} \|\bar{\varphi}_k - \bar{\varphi}_\star\|_{L^2(\mu_\star)}^2 - O(\epsilon), \end{aligned} \tag{36}$$

where $\sigma := e^{-6\|c_\epsilon\|_\infty}$, and the last inequality follows by Eq.(34) and boundedness of $\bar{\psi}_k$ and $\bar{\psi}_\star$ in Lemma 4. For the first integral, $\int_{\Omega} \partial_1 G(\bar{\varphi}_{k+1}, \bar{\psi}_k)(\mathbf{x}) [\bar{\varphi}_k(\mathbf{x}) - \bar{\varphi}_\star(\mathbf{x})] \mu_\star(d\mathbf{x}) = O(\epsilon)$ because $\partial_1 G(\bar{\varphi}_{k+1}, \bar{\psi}_k)(\mathbf{x})$ includes a deterministic scalar and a small perturbation with $\mu_\star(\bar{\varphi}_k(\mathbf{x})) = \mu_\star(\bar{\varphi}_\star(\mathbf{x})) = 0$.

Hence

$$\begin{aligned} & \int_{\Omega} \partial_1 G(\bar{\varphi}_k, \bar{\psi}_k)(\mathbf{x}) [\bar{\varphi}_k(\mathbf{x}) - \bar{\varphi}_\star(\mathbf{x})] \mu_\star(d\mathbf{x}) \\ &= \int_{\Omega} [\partial_1 G(\bar{\varphi}_k, \bar{\psi}_k)(\mathbf{x}) - \partial_1 G(\bar{\varphi}_{k+1}, \bar{\psi}_k)(\mathbf{x})] [\bar{\varphi}_k(\mathbf{x}) - \bar{\varphi}_\star(\mathbf{x})] \mu_\star(d\mathbf{x}) + O(\epsilon) \\ & \geq -\frac{1}{2\sigma} \|\partial_1 G(\bar{\varphi}_k, \bar{\psi}_k) - \partial_1 G(\bar{\varphi}_{k+1}, \bar{\psi}_k)\|_{L^2(\mu_\star)}^2 - \frac{\sigma}{2} \|\bar{\varphi}_k(\mathbf{x}) - \bar{\varphi}_\star(\mathbf{x})\|_{L^2(\mu_\star)}^2 + O(\epsilon), \end{aligned} \tag{37}$$

where the inequality follows from Hölder's inequality and Young's inequality.

Plugging Eq.(37) into Eq.(36), we have

$$G(\bar{\varphi}_\star, \bar{\psi}_\star) - G(\bar{\varphi}_k, \bar{\psi}_k) \leq \frac{1}{2\sigma} \|\partial_1 G(\bar{\varphi}_k, \bar{\psi}_k) - \partial_1 G(\bar{\varphi}_{k+1}, \bar{\psi}_k)\|_{L^2(\mu_\star)}^2 + O(\epsilon). \tag{38}$$

Note that

$$\begin{aligned} |\partial_1 G(\bar{\varphi}_k, \bar{\psi}_k)(\mathbf{x}) - \partial_1 G(\bar{\varphi}_{k+1}, \bar{\psi}_k)(\mathbf{x})| & \leq \int_{\Omega} \left| e^{\bar{\varphi}_{k+1} \oplus \bar{\psi}_k - c_\epsilon} - e^{\bar{\varphi}_k \oplus \bar{\psi}_k - c_\epsilon} \right| \nu_\star(d\mathbf{y}) \\ & \leq e^{6\|c_\epsilon\|_\infty} \int_{\Omega} |\bar{\varphi}_{k+1} \oplus \bar{\psi}_k - \bar{\varphi}_k \oplus \bar{\psi}_k| \nu_\star(d\mathbf{y}) \\ & = \frac{1}{\sigma} |\bar{\varphi}_{k+1}(\mathbf{x}) - \bar{\varphi}_k(\mathbf{x})|, \end{aligned} \tag{39}$$

where the second inequality follows by Lemma 4 and the exponential function follows a Lipschitz continuity such that: $e^a - e^b \leq e^M |b - a|$ for $a, b \leq M$; $\sigma := e^{-6\|c_\epsilon\|_\infty}$.

First combining Eq.(38) and (39) and then including Lemma 6, we conclude that

$$\begin{aligned} G(\bar{\varphi}_*, \bar{\psi}_*) - G(\bar{\varphi}_k, \bar{\psi}_k) &\leq \frac{1}{2\sigma^3} \|\bar{\varphi}_{k+1} - \bar{\varphi}_k\|_{L^2(\mu_*)}^2 + O(\epsilon) \\ &\leq \frac{1}{\sigma^4} (G(\bar{\varphi}_{k+1}, \bar{\psi}_{k+1}) - G(\bar{\varphi}_k, \bar{\psi}_k)) + \frac{O(\epsilon)}{\sigma^4}, \end{aligned}$$

where the last inequality follows by $\sigma \leq 1$. Further writing $\Delta_k = G(\bar{\varphi}_*, \bar{\psi}_*) - G(\bar{\varphi}_k, \bar{\psi}_k)$, we have

$$\Delta_k \leq \frac{1}{\sigma^4} (\Delta_k - \Delta_{k+1}) + \frac{O(\epsilon)}{\sigma^4}.$$

In other words, we can derive the contraction property as follows

$$\Delta_{k+1} \leq (1 - \sigma^4)\Delta_k + O(\epsilon) \leq \dots \leq (1 - \sigma^4)^{k+1}\Delta_0 + O(e^{24\|c_\epsilon\|_\infty}\epsilon),$$

which hereby completes the claim of the theorem for any $k \geq 1$. \square

Part II: Convergence of the Potentials

For the convergence of the potential function, in spirit to Lemma 6, we obtain

$$G_*(\bar{\varphi}_*, \bar{\psi}_*) - G(\bar{\varphi}_k, \bar{\psi}_k) := \Delta_k \geq \frac{\sigma}{2} \left(\|\bar{\varphi}_* - \bar{\varphi}_k\|_{L^2(\mu_*)}^2 + \|\bar{\psi}_* - \bar{\psi}_k\|_{L^2(\nu_*)}^2 \right) - O(\epsilon).$$

We can upper bound the potential as follows

$$\|\bar{\varphi}_* - \bar{\varphi}_k\|_{L^2(\mu_*)}^2 + \|\bar{\psi}_* - \bar{\psi}_k\|_{L^2(\nu_*)}^2 \leq \frac{2}{\sigma}\Delta_k + \frac{O(\epsilon)}{\sigma} \leq \frac{2}{\sigma}(1 - \sigma^4)^k\Delta_0 + O(e^{30\|c_\epsilon\|_\infty}\epsilon).$$

Further applying $(|a| + |b|)^2 \leq 2a^2 + 2b^2$ and $\sqrt{c^2 + d^2} \leq |c| + |d|$, we have

$$\begin{aligned} \|\bar{\varphi}_* - \bar{\varphi}_k\|_{L^2(\mu_*)} + \|\bar{\psi}_* - \bar{\psi}_k\|_{L^2(\nu_*)} &\leq \sqrt{\frac{4}{\sigma}(1 - \sigma^4)^{k+1}\Delta_0 + O(e^{15\|c_\epsilon\|_\infty}\epsilon^{1/2})} \\ &\lesssim e^{3\|c_\epsilon\|_\infty}\beta_\epsilon^{\frac{k}{2}} + e^{15\|c_\epsilon\|_\infty}\epsilon^{1/2}, \end{aligned} \tag{40}$$

where $\beta_\epsilon = 1 - \sigma^4 = 1 - e^{-24\|c_\epsilon\|_\infty}$. \square

9.2 Convergence of the Static Couplings

Proof of Theorem 2

Recall from the bounded potential in Lemma 4, we have

$$e^{\bar{\varphi}_* \oplus \bar{\psi}_* - c_\epsilon} - e^{\bar{\varphi}_k \oplus \bar{\psi}_k - c_\epsilon} \leq e^{6\|c_\epsilon\|_\infty} (|\bar{\varphi}_* - \bar{\varphi}_k| + |\bar{\psi}_* - \bar{\psi}_k|). \tag{41}$$

Following Theorem 3 of Deligiannidis et al. [2021], we define a class of 1-Lipschitz functions $\text{Lip}_1 = \{F \mid |F(\mathbf{x}_0, \mathbf{y}_0) - F(\mathbf{x}_1, \mathbf{y}_1)| \leq \|\mathbf{x}_1 - \mathbf{x}_0\|_2 + \|\mathbf{y}_1 - \mathbf{y}_0\|_2\}$. Since the structural property (10) allows to represent π_* using $(\varphi_* + a) \oplus (\psi_* - a)$ for any a . For any $F \in \text{Lip}_1$, we have

$$\begin{aligned} &\iint_{X \times Y} F e^{\bar{\varphi}_* \oplus \bar{\psi}_* - c_\epsilon} d(\mu_* \otimes \nu_*) - \iint_{X \times Y} F e^{\bar{\varphi}_k \oplus \bar{\psi}_k - c_\epsilon} d(\mu_{*,k} \otimes \nu_{*,k}) \\ &\leq \iint_{X \times Y} F e^{\bar{\varphi}_* \oplus \bar{\psi}_* - c_\epsilon} d(\mu_* \otimes \nu_*) - \iint_{X \times Y} F e^{\bar{\varphi}_k \oplus \bar{\psi}_k - c_\epsilon} d(\mu_* \otimes \nu_*) \\ &\quad + \iint_{X \times Y} F e^{\bar{\varphi}_k \oplus \bar{\psi}_k - c_\epsilon} d(\mu_* \otimes \nu_*) - \iint_{X \times Y} F e^{\bar{\varphi}_k \oplus \bar{\psi}_k - c_\epsilon} d(\mu_{*,k} \otimes \nu_{*,k}) \\ &\leq \iint_{X \times Y} F \underbrace{|e^{\bar{\varphi}_* \oplus \bar{\psi}_* - c_\epsilon} - e^{\bar{\varphi}_k \oplus \bar{\psi}_k - c_\epsilon}|}_{\text{by Eq.(41)}} d(\mu_* \otimes \nu_*) \\ &\quad + \iint_{X \times Y} F e^{\bar{\varphi}_k \oplus \bar{\psi}_k - c_\epsilon} d(\mu_* \otimes |\nu_* - \nu_{*,k}| + |\mu_* - \mu_{*,k}| \otimes \nu_{*,k}) \\ &\lesssim e^{9\|c_\epsilon\|_\infty}\beta^{k/2} + e^{21\|c_\epsilon\|_\infty}\epsilon^{1/2}, \end{aligned}$$

where the last inequality is mainly derived from the first term in the second inequality by combining (40) and (41); the second term in the second inequality can be upper bounded by Lemma 7.

Recall the definition of the duality of the 1-Wasserstein distance, we have

$$\begin{aligned} \mathbf{W}_1(\pi_k, \pi_\star) &= \sup \left\{ \iint_{X \times Y} F e^{\bar{\varphi}_\star \oplus \bar{\psi}_\star - c_\epsilon} d(\mu_\star \otimes \nu_\star) \right. \\ &\quad \left. - \iint_{X \times Y} F e^{\bar{\varphi}_k \oplus \bar{\psi}_k - c_\epsilon} d(\mu_{\star,k} \otimes \nu_{\star,k}) : F \in \text{Lip}_1 \right\} \\ &\leq O(e^{9\|c_\epsilon\|_\infty} \beta^{k/2} + e^{21\|c_\epsilon\|_\infty} \epsilon^{1/2}). \end{aligned}$$

□

9.3 Auxiliary Results

Lemma 7. *Given probability densities $\rho(\mathbf{x}) = e^{-U(\mathbf{x})}/\mathbb{Z}$ and $\tilde{\rho}(\mathbf{x}) = e^{-\tilde{U}(\mathbf{x})}/\tilde{\mathbb{Z}}$ defined on Ω , where Ω is a bounded domain that contains Ω and Ω , \mathbb{Z} and $\tilde{\mathbb{Z}}$ are the normalizing constants. For small enough $\epsilon \lesssim \frac{1}{(D+1)^2}$, where D is the radius of a centered ball covering Ω , we have*

$$1 - O(\epsilon) \leq \frac{\rho(\mathbf{x})}{\tilde{\rho}(\mathbf{x})} \leq 1 + O(\epsilon), \quad 1 - O(\epsilon) \leq \frac{\tilde{\rho}(\mathbf{x})}{\rho(\mathbf{x})} \leq 1 + O(\epsilon). \quad (42)$$

Proof

From the approximation assumption A4: $\|\nabla \tilde{U}(\mathbf{x}) - \nabla U(\mathbf{x})\|_2 \leq \epsilon(1 + \|\mathbf{x}\|_2)$.

Moreover, U satisfies the smoothness assumption A3. Note that for any $\mathbf{x}, \mathbf{y} \in \Omega$

$$U(\mathbf{x}) - U(\mathbf{y}) = \int_0^1 \frac{d}{dt} U(t\mathbf{x} + (1-t)\mathbf{y}) = \int_0^1 \langle \mathbf{x} - \mathbf{y}, \nabla U(t\mathbf{x} + (1-t)\mathbf{y}) \rangle dt.$$

Moreover, there exist \mathbf{x}_0 such that $U(\mathbf{x}_0) = \tilde{U}(\mathbf{x}_0)$ since ρ and $\tilde{\rho}$ are probability densities. It follows

$$\begin{aligned} |\tilde{U}(\mathbf{x}) - U(\mathbf{x})| &= \left| \int_0^1 \langle \mathbf{x} - \mathbf{x}_0, \nabla \tilde{U}(\dot{\mathbf{x}}_t) - \nabla U(\dot{\mathbf{x}}_t) \rangle dt \right| \\ &\leq \int_0^1 \|\mathbf{x} - \mathbf{x}_0\|_2 \cdot \|\nabla \tilde{U}(\dot{\mathbf{x}}_t) - \nabla U(\dot{\mathbf{x}}_t)\|_2 dt \\ &\leq \epsilon(\|\mathbf{x}\|_2 + \|\mathbf{x}_0\|_2)(1 + \|\mathbf{x}\|_2) \lesssim \epsilon(D+1)^2, \end{aligned}$$

where $\dot{\mathbf{x}}_t = t\mathbf{x} + (1-t)\mathbf{x}_0$ is a line from \mathbf{x}_0 to \mathbf{x} .

For the normalizing constant, we have

$$|\tilde{\mathbb{Z}} - \mathbb{Z}| \leq \int_{\Omega} e^{-U(\mathbf{x})} |e^{-\tilde{U}(\mathbf{x})+U(\mathbf{x})} - 1| d\mathbf{x} \lesssim \epsilon \int_{\Omega} e^{-U(\mathbf{x})} \epsilon(D+1)^2 d\mathbf{x},$$

where the last inequality follows by Eq.(9.3) and $e^a \leq 1 + 2a$ for $a \in [0, 1]$. We deduce

$$\left| \log \frac{\rho(\mathbf{x})}{\tilde{\rho}(\mathbf{x})} \right| = \left| \tilde{U}(\mathbf{x}) - U(\mathbf{x}) + \log \frac{\tilde{\mathbb{Z}}}{\mathbb{Z}} \right| \leq O(\epsilon).$$

□

Notably, the above lemma also implies that $\text{KL}(\rho \|\tilde{\rho}) \leq O(\epsilon)$ and $\text{KL}(\tilde{\rho} \|\rho) \leq O(\epsilon)$.

9.4 Connections between dual optimization and projections

To see why (12b) holds. We first denote the second marginal of $d\pi(\varphi_k, \psi_k) := e^{\varphi_k \oplus \psi_k} d\mathcal{G}$ by ν' and then proceed to show $\nu' = \nu_\star$ [Nutz, 2022]. Recall that G is concave and $\psi_k = \arg \max_{\psi \in L^1(\nu_\star)} G(\varphi_k, \psi)$, it suffices to show that given fixed $\varphi_k \in L^1(\mu_\star)$, $\psi_k \in L^1(\nu_\star)$, a constant η and bounded measurable function $\delta_\psi : \mathbb{R}^d \rightarrow \mathbb{R}$, the maximality of $G(\varphi_k, \psi_k)$ implies

$$0 = \frac{d}{d\eta} \Big|_{\eta=0} G(\varphi_k, \psi_k + \eta \delta_\psi) = \nu_\star(\delta_\psi) - \iint_{\Omega^2} \delta_\psi e^{\varphi_k \oplus \psi_k} d\mathcal{G} = \nu_\star(\delta_\psi) - \nu'(\delta_\psi).$$

Hence $\nu' = \nu_\star$. Similarly, we can show (12a).

9.5 Connections between Static Primal IPF (9) and Static Dual IPF (13)

It suffices to show the equivalence between $\pi_{2k} = \arg \min_{\pi \in \Pi(\cdot, \nu_*)} \text{KL}(\pi \| \pi_{2k-1})$ and $\psi_k(\mathbf{y}) = -\log \int_{\Omega} e^{\varphi_k(\mathbf{x}) - c_\varepsilon(\mathbf{x}, \mathbf{y})} \mu_*(d\mathbf{x})$.

For any $\pi_{2k} \in \Pi(\cdot, \nu_*)$, we invoke the disintegration of measures and obtain $\pi_{2k} = K^\? \otimes \nu_*$. In addition, we have $\pi_{2k-1} = K \otimes \nu'$. Now we can formulate

$$\text{KL}(\pi \| \pi_{2k-1}) = \text{KL}(\nu_* \| \nu') + \text{KL}(K^\? \| K).$$

The conditional probability of π_{2k-1} given \mathbf{y} is a normalized probability such that

$$\frac{\frac{d\pi_{2k-1}}{d\mu_* \otimes \nu_*}}{\int \frac{d\pi_{2k-1}}{d\mu_* \otimes \nu_*} d\mu_*} = \frac{dK}{d\mu_*}(\mathbf{x}, \mathbf{y}) = \frac{e^{\varphi_k \oplus \psi_{k-1} - c_\varepsilon}}{\int e^{\varphi_k \oplus \psi_{k-1} - c_\varepsilon} d\mu_*} = \frac{e^{\varphi_k - c_\varepsilon}}{\int e^{\varphi_k - c_\varepsilon} d\mu_*}.$$

The minimizer is achieved by setting $K^\? = K$, namely $\pi_{2k} = K \otimes \nu$. It follows that

$$\frac{d\pi_{2k}}{d(\mu_* \otimes \nu_*)} = \frac{d(K \otimes \nu_*)}{d(\mu_* \otimes \nu_*)} = \frac{e^{\varphi_k - c_\varepsilon}}{\int e^{\varphi_k - c_\varepsilon} d\mu_*} := e^{\varphi_k \oplus \psi_k - c_\varepsilon}.$$

In other words, we have $\psi_k(\mathbf{y}) = -\log \int_{\Omega} e^{\varphi_k(\mathbf{x}) - c_\varepsilon(\mathbf{x}, \mathbf{y})} \mu_*(d\mathbf{x})$, which verifies the connections.

10 Experimental Details

Reflection Implementations Lou and Ermon [2023] already gave a nice tutorial on the implementation of hypercube-related domains with image applications. For extensions to general domains, we provide our solutions in Algorithm 4. The *crucial component* is a *Domain Checker* to verify if a point is inside or outside of a domain, and it appears to be quite computationally expensive. To solve this problem, we propose two solutions :

- 1) If there exists a computationally efficient conformal map that transforms a manifold into simple shapes, such as a sphere or square, we can apply simple rules to conclude if a proposal is inside a domain.
- 2) If the first solution is expensive, we can **cache** the domain through a fine-grid mesh $\{X_{i,j,\dots}\}_{i,j,\dots}$. Then, we approximate the condition via

$$\min_{i,j,\dots} \text{Distance}(\tilde{\mathbf{x}}_{k-1}, \{X_{i,j,\dots}\}_{i,j,\dots}) \leq \text{threshold}.$$

With the parallelism in Torch or JAX, the above calculation can be quite efficient. Nevertheless, a finer grid leads to a higher accuracy but also induces more computations. We can also expect the curse of dimensionality in ultra-high-dimensional problems and simpler domains are more preferred in such cases. Moreover, if $\mathbf{x}_{k+1} \notin \Omega$ in extreme cases, one may consider ad-hoc rules with an error that decreases as we anneal the learning rate. Other elegant solutions include slowing down the process near the boundary or warping the geometry with a Riemannian metric [Fishman et al., 2023].

Algorithm 4 Practical Reflection Operator

Simulate a proposal $\tilde{\mathbf{x}}_{k+1}$ via an SDE given $\mathbf{x}_k \in \Omega$.

if Domain Checker: $\tilde{\mathbf{x}}_{k+1} \in \Omega$ **then**

Set $\mathbf{x}_{k+1} = \tilde{\mathbf{x}}_{k+1}$

else

Search (binary) the boundary $\dot{\mathbf{x}}_{k+1} \in \partial\Omega$, where $\dot{\mathbf{x}}_{k+1} = \eta\mathbf{x}_k + (1 - \eta)\tilde{\mathbf{x}}_{k+1}$ for $\eta \in (0, 1)$.

Compute $\boldsymbol{\nu} = \dot{\mathbf{x}}_{k+1} - \tilde{\mathbf{x}}_{k+1}$ and the unit normal vector \mathbf{n} associated with $\dot{\mathbf{x}}_{k+1}$.

Set $\mathbf{x}_{k+1} = \dot{\mathbf{x}}_{k+1} + \boldsymbol{\nu} - 2\langle \boldsymbol{\nu}, \mathbf{n} \rangle \mathbf{n}$.

end if

10.1 Domains of 2D Synthetic Data

We consider input $t \in [0, 1]$ and output $(x, y) \in \mathbb{R}^2$. The normal vector can be derived accordingly.

Table 2: Densities using (relected) Langevin diffusion with a practical running time and infinite time.

SDE	Practical Time	Infinite Time	SDE	Practical Time	Infinite Time
VP	Approx. Gaussian	Gaussian	RVP	Approx. Truncated Gaussian	Truncated Gaussian
VE	Approx. Gaussian	Uniform	RVE	Approx. Truncated Uniform	Truncated Uniform

Flower (petals $p = 5$ and move out length $m = 3$)

$$r = \sin(2\pi pt) + m, \quad x = r \cos(2\pi t), \quad y = r \sin(2\pi t).$$

Heart

$$x = 16 \sin(2\pi t)^3, \quad y = 13 \cos(2\pi t) - 5 \cos(4\pi t) - 2 \cos(6\pi t) - \cos(8\pi t).$$

Octagon ($c + 1$ edges $(X_i, Y_i)_{i=0}^c$ with $(X_c, Y_c) = (X_0, Y_0)$)

$$r = ct - \lfloor ct \rfloor; \quad x = (1 - r) \cdot X_{\lfloor ct \rfloor} + r \cdot X_{\lfloor ct \rfloor + 1}; \quad y = (1 - r) \cdot Y_{\lfloor ct \rfloor} + r \cdot Y_{\lfloor ct \rfloor + 1}.$$

10.2 How to initialize: Warm-up Study

Consider a Langevin diffusion (LD) and a reflected Langevin (RLD) with score functions S_1 and S_2 :

$$\begin{aligned} \text{LD} : \quad & d\mathbf{x}_t = S_1(\mathbf{x}_t)dt + d\mathbf{w}_t, & \mathbf{x}_t \in \mathbb{R}^d \\ \text{RLD} : \quad & d\mathbf{x}_t = S_2(\mathbf{x}_t)dt + d\mathbf{w}_t + \mathbf{n}(\mathbf{x})d\mathbf{L}_t, & \mathbf{x}_t \in \Omega. \end{aligned}$$

LD converges to $\mu_1 \propto e^{S_1(\mathbf{x})}$ and RLD converges to $\mu_2 \propto e^{S_2(\mathbf{x})} \mathbf{1}_{\mathbf{x} \in \Omega}$ [Bubeck et al., 2018, Lamperski, 2021] as $t \rightarrow \infty$. In other words, inheriting the score function S_1 from LD to RLD (by setting $S_1 = S_2$) yields the desired invariant distribution $\mu_1 \mathbf{1}_{\mathbf{x} \in \Omega}$.

Denote by RVP (or RVE) the VP-SDE (or VE-SDE) in reflected SB. One can easily show in Table 2 that VP (or RVP) converges approximately to a (or truncated) Gaussian prior within a practical training time, which implies an *unconstrained VP-SDE diffusion model is a good warm-up candidate* for reflected SB. Empirically, we are able to verify this fact through 2D synthetic data.

However, this may not be the case for VE because it converges to a uniform measure in \mathbb{R}^d but only obtains an approximate Gaussian in a short time. By contrast, RVE converges to the invariant uniform distribution much faster because it doesn't need to fully explore \mathbb{R}^d . This implies *initializing the score function from VE-based diffusion models for reflected SB may not be a good choice*. Instead, we use RVE-based diffusion models [Lou and Ermon, 2023] as the warm-up.

10.3 Generation of Image Data

Datasets. Both CIFAR-10 and ImageNet 64×64 are obtained from public resources. All RGB values are between $[0, 1]$. The domain is $\Omega = [0, 1]^d$, where $d = 3 \times 32 \times 32$ for the CIFAR-10 task, $d = 3 \times 64 \times 64$ for the ImageNet task, $d = 1 \times 32 \times 32$ for the MNIST task.

SDE. We use reflected VESDE for the reference process due to its simplicity [Lou and Ermon, 2023], and it helps with facilitating the warmup training. The SDE is discretized into 1000 steps. The initial and the terminal scale of the diffusion are $\sigma_{\min} = 0.01$ and $\sigma_{\max} = 5$ respectively. The prior reference is set as the uniform distribution on Ω .

Training. The alternate training Algorithm 1 can be accelerated with proper initialization, and the pre-training of the backward score model is critical for successfully training the model. At the warmup phase, the forward score is set as zero and only the backward score model is trained by inheriting the setup in the reflected SGM [Lou and Ermon, 2023]. The learning rate is 10^{-5} . To improve the training efficiency and stabilize the full path-based training target in Algorithm 1, We use Exponential Moving Average (EMA) in the training with the decay rate of 0.99 [Hyvärinen, 2005, Vahdat et al., 2021, Lou and Ermon, 2023].

Neural networks. As the high accuracy inference task relies more on the backward score model than the forward score model, the backward process is equipped with more advanced and larger structure. The backward score function uses NCSN++ [Song et al., 2021b] for the CIFAR-10 task and ADM [Dhariwal and Nichol, 2022] for the ImageNet task. The NCSN++ network has 107M parameters. The ADM network has 295M parameters. For MNIST, a smaller U-Net structure with 1.3M parameters (2 attention heads per attention layer, 1 residual block per downsample, 32 base

channels) is used for both forward and backward processes. Many previous studies have verified the success of these neural networks in the diffusion based generative tasks [Song et al., 2021b, Lou and Ermon, 2023, Chen et al., 2022b]. The forward score function is modeled using a simpler U-Net with 62M parameters.

Inference. In both CIFAR-10 and ImageNet 64×64 tasks, images are generated unconditionally, and the quality of the samples is evaluated using Frechet Inception Distance (FID) over 50,000 samples [Heusel et al., 2017, Song et al., 2021b]. In MNIST, the the quality of the samples is evaluated using Negative Log-Likelihood (NLL). Predictor-Corrector using reflected Langevin dynamics is used to further improve the result which does not require any change of the model structure [Song et al., 2021b, Chen et al., 2022b, Lou and Ermon, 2023, Bubeck et al., 2018].

$$\mathbf{x}'_t = \text{reflection}\left(\mathbf{x}_t + \sigma_t \mathbf{s}(t, \mathbf{x}_t) + \sqrt{2\sigma_t} \varepsilon\right), \quad \varepsilon \sim N(\mathbf{0}, I)$$

$$\mathbf{s}(t, \mathbf{x}_t) = \frac{1}{g} [\overrightarrow{\mathbf{z}}_t^\theta(t, \mathbf{x}_t) + \overleftarrow{\mathbf{z}}_t^\omega(t, \mathbf{x}_t)], \quad \sigma_t = \frac{2r_{\text{SNR}}^2 g^2 \|\varepsilon\|^2}{\|\mathbf{s}(t, \mathbf{x}_t)\|^2}$$

where $\overrightarrow{\mathbf{z}}_t^\theta, \overleftarrow{\mathbf{z}}_t^\omega$ are the backward and forward score functions as in Algorithm 1.

The likelihood of the diffusion model follows the probabilistic flow neural ODE [Song et al., 2021b, Chen et al., 2022b, Lou and Ermon, 2023]

$$d\mathbf{x}_t = [f(\mathbf{x}_t, t) - \frac{1}{2}g(t)^2 \mathbf{s}(t, \mathbf{x}_t)] dt := \tilde{f}(\mathbf{x}_t, t) dt$$

$$\log p_0(\mathbf{x}_0) = \log p_T(\mathbf{x}_T) + \int_0^T \nabla \cdot \tilde{f}(\mathbf{x}_t, t) dt$$

10.4 Optimal Transport May Help Reduce NFEs

To demonstrate the effectiveness of OT in reducing the number of function evaluations (NFEs), we study generations based on different NFEs on a simulation example and the MNIST dataset and compare the reflected Schrödinger bridge with reflected diffusion (implicit) [Fishman et al., 2023]. We use the same setup (e.g. implicit training loss with the same training budget) to be consistent except that reflected SB uses a well-optimized forward network $\overrightarrow{\mathbf{z}}_t^\theta$ to train the backward network $\overleftarrow{\mathbf{z}}_t^\omega$ while reflected diffusion can be viewed as the first stage of SB training by fixing $\overrightarrow{\mathbf{z}}_t^\theta \equiv \mathbf{0}$.

We observe in Figure 7 that in the regime of NFE=20, both reflected diffusion (implicit) and reflected SB demonstrate remarkable performance in the simulation example. Despite the inherent compromise in sample quality with smaller NFEs, our investigation revealed that a well-optimized $\overrightarrow{\mathbf{z}}_t^\theta$ significantly contributes to training $\overleftarrow{\mathbf{z}}_t^\omega$ compared to the baseline with $\overrightarrow{\mathbf{z}}_t^\theta \equiv \mathbf{0}$, leading to an improved sample quality even in cases where NFE is set to 10 and 12. Similar findings are observed in the MNIST dataset in Figure 8. We use the same setup as before, finding NFE=100 delivers reasonable performance in both reflected diffusion (implicit) and reflected SB. Decreasing NFE to 50 shows slightly stronger performance retention in reflected SB.

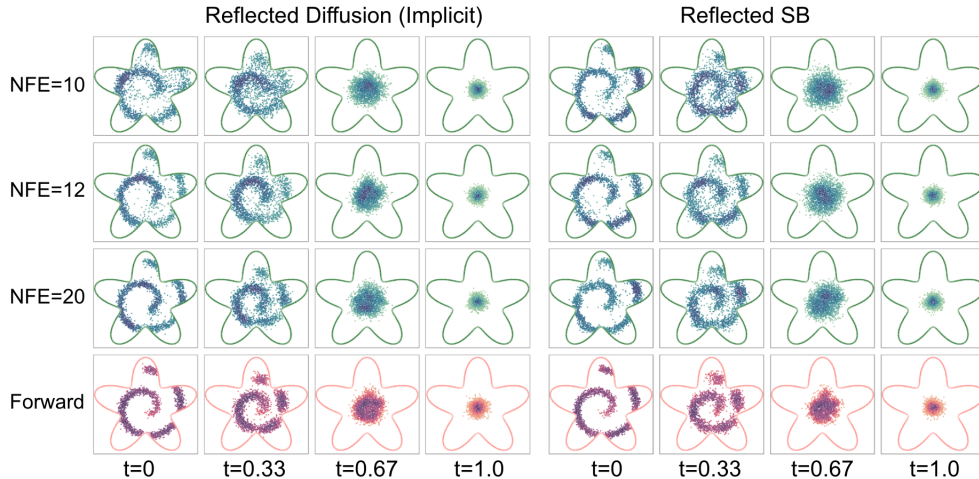


Figure 7: Reflected Schrödinger bridge v.s. reflected diffusion (implicit) based on different NFEs.

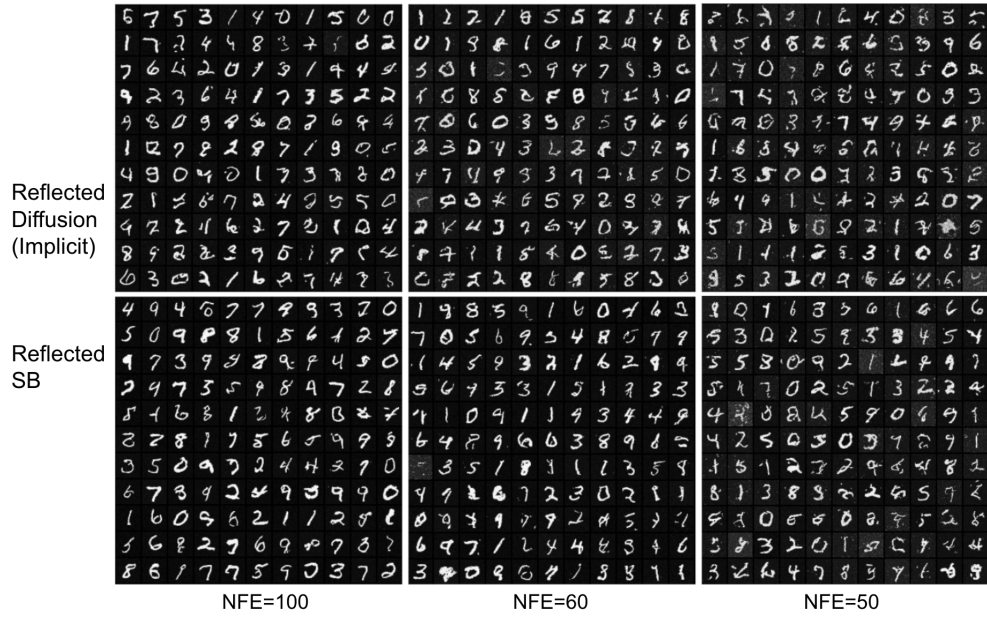


Figure 8: Reflected Schrödinger bridge v.s. reflected diffusion (implicit) based on MNIST

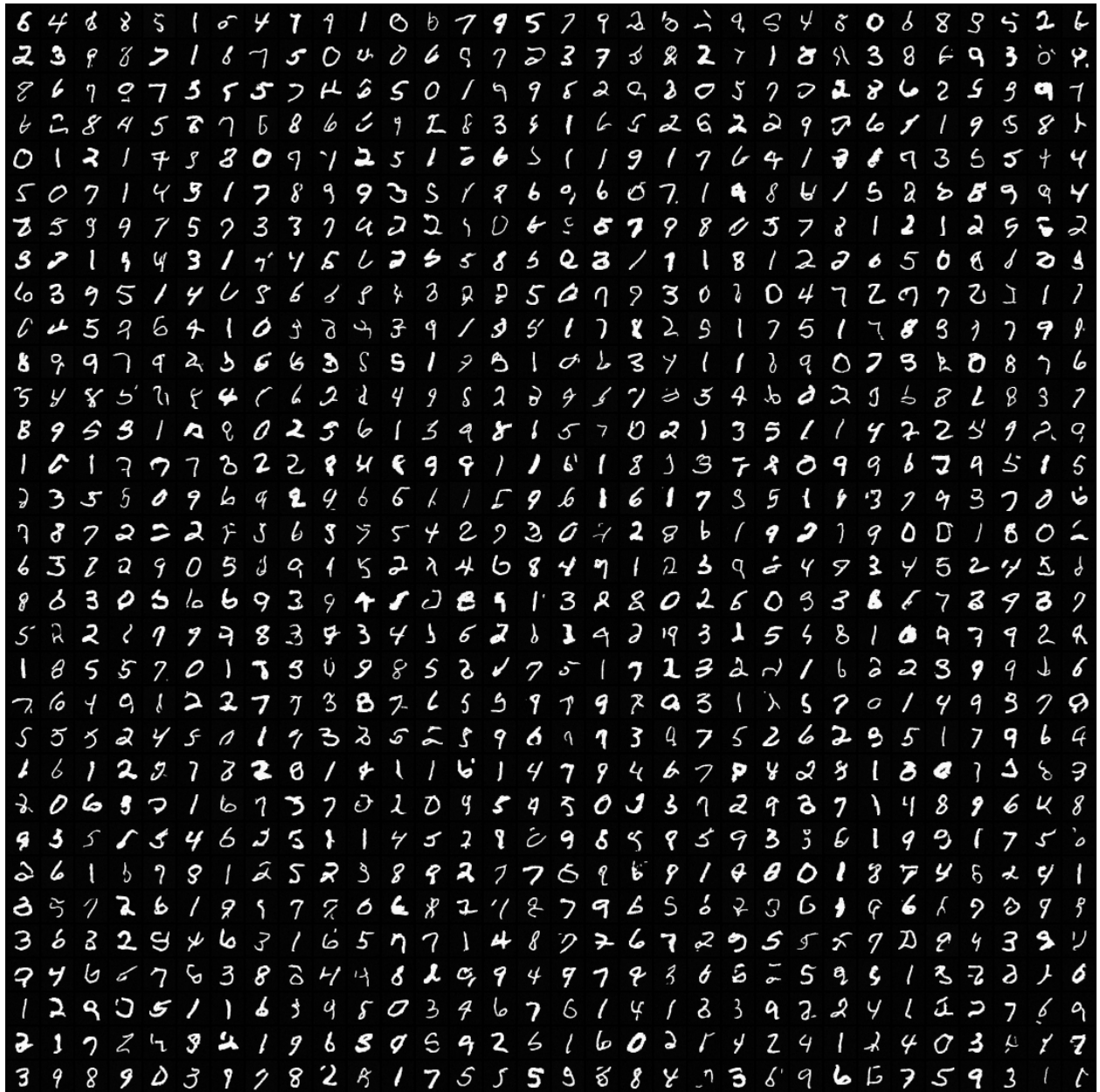


Figure 9: Generated samples via reflected SB on MNIST.

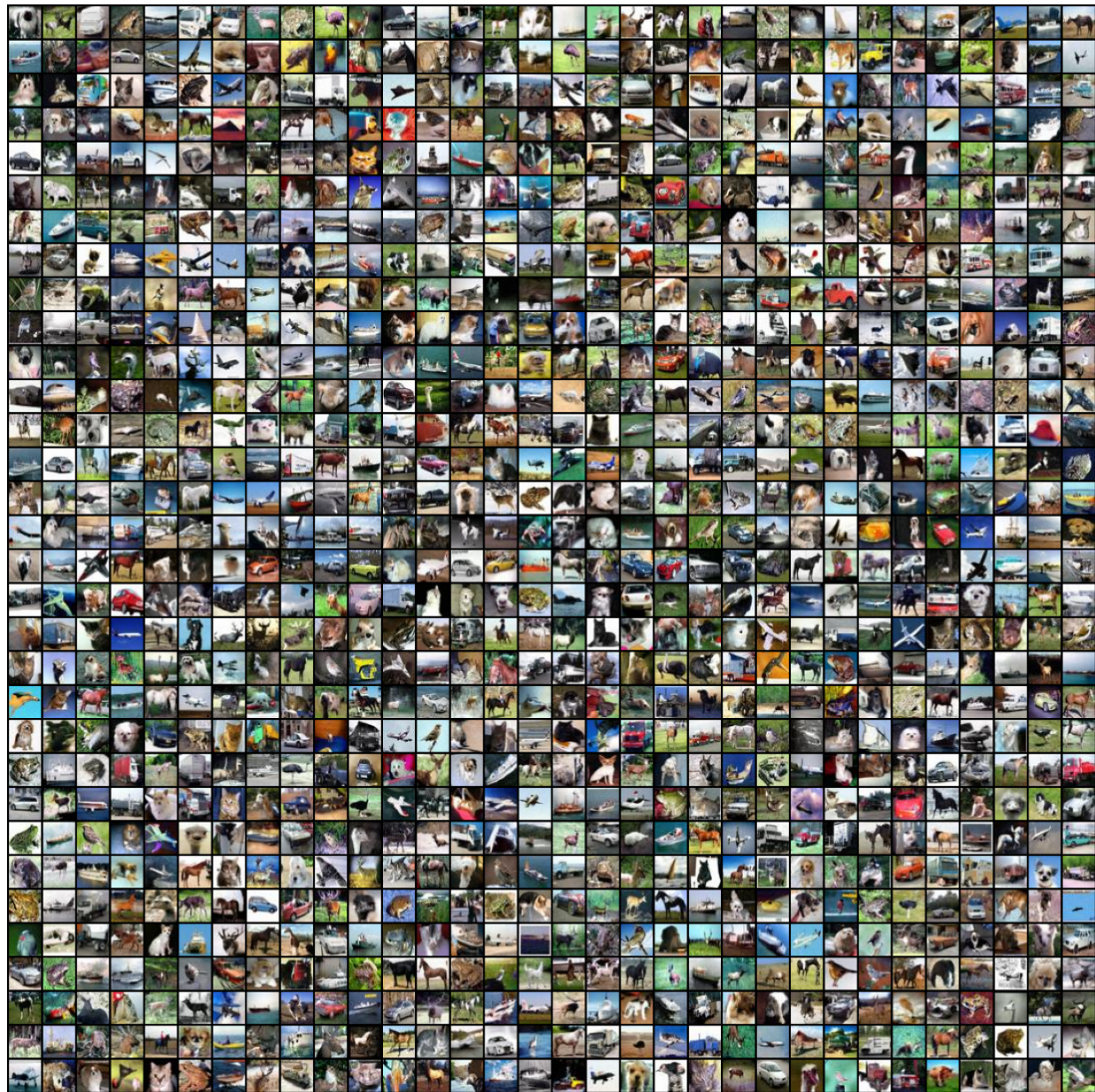


Figure 10: Generated samples via reflected SB on CIFAR-10.

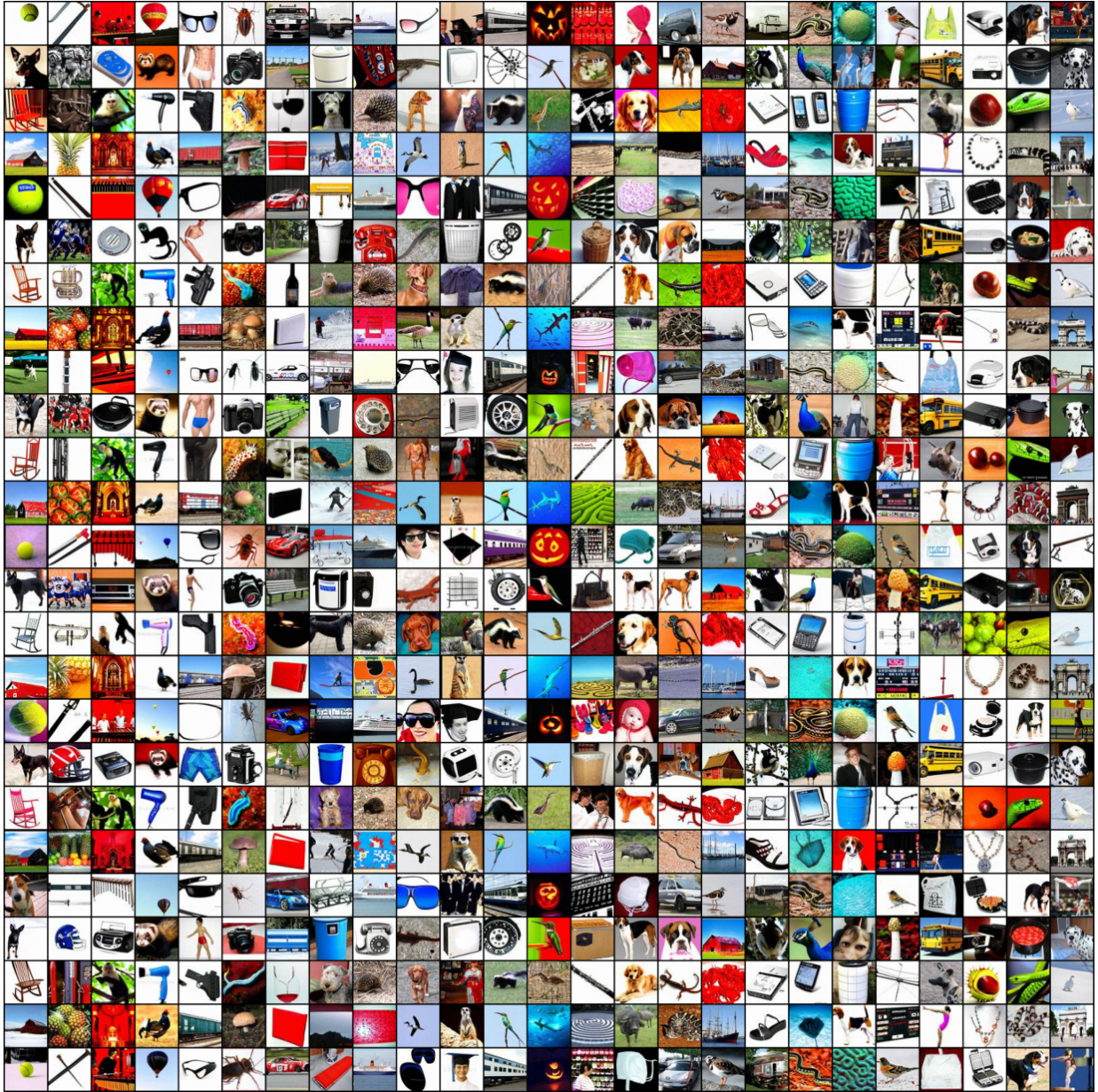


Figure 11: Generated samples via reflected SB on ImageNet-64.